Radio-wave depolarization and scattering within ice sheets: a matrix-based model to link radar and ice-core measurements and its application

Shuji FUJITA,[1] Hideo MAENO,[2] Kenichi MATSUOKA[3]

[1]*National Institute of Polar Research, Kaga 1-9-10, Itabashi-ku, Tokyo 173-8515, Japan*
E-mail: sfujita@pmg.nipr.ac.jp
[2]*National Institute of Information and Communications Technology, Nukui-kita, Koganei, Tokyo 184-8795, Japan*
[3]*Department of Earth and Space Sciences, University of Washington, Seattle, Washington 98195-1310, USA*

ABSTRACT. Crystal-orientation fabric (COF) has a large influence on ice-sheet flow. Earlier radar studies have shown that COF-based birefringence occurs within ice sheets. Radio-wave scattering in polar ice results from changing physical properties of permittivity and conductivity that arise from differing values of density, acidity and COF. We present an improved mathematical model that can handle all these phenomena together. We use this matrix-based model to study the two-way propagation of depolarized radio waves that scatter at both isotropic and anisotropic boundaries. Based on numerical simulations, we demonstrate how COF affects the radar signals in terms of radar polarization and frequency. We then compare the simulated features with VHF radar data obtained at two contrasting inland sites in East Antarctica, where COF is known from ice-core studies. These two sites are Dome Fuji, located near a dome summit, and Mizuho, located in a converging ice-flow region. Data at Dome Fuji are dominated by typical features resulting from birefringence. In contrast, both birefringence and anisotropic scattering affect the radar data at Mizuho. We argue that radar methods can be used to determine principal axes and strength of birefringence in the ice sheets.

1. INTRODUCTION

Understanding the physical and chemical characteristics of polar ice sheets is important for determining how such huge ice masses have responded to past climate change and how they will respond to present and future climatic changes. Studies with radar over the past few decades using a wide range of frequencies have shown that radar is a powerful tool for investigating the internal structure of large ice masses (e.g. Robin and others, 1969; Bogorodsky and others, 1985; Gogineni and others, 1998; Matsuoka and others, 2003).

Among ice characteristics, the crystal-orientation fabric (COF) has a large influence on the flow of ice sheets. This is because ice flow generates various types of COF, which in turn affect the ice viscosity, and thus ice flow, in various ways (e.g. Budd and Jacka, 1989; Azuma, 1994). Our current understanding of COF is based on a limited number of ice cores, which altogether amount to a tiny volume in comparison to the vast ice sheets. Furthermore, COF data usually come from selected depth segments, as high-resolution continuous measurements are extremely time-consuming. Detailed study of spatial variability of COF is not available from ice cores. If radar-sounding methods can detect information related to COF, it should be a viable way to investigate the spatial distribution and changes in COF within the vast ice sheets. Testing this suggestion is the topic of this paper.

Single crystals of ice have dielectric permittivity tensor, $\boldsymbol{\varepsilon}'_{\mathrm{p}}$, in the principal coordinate,

$$\boldsymbol{\varepsilon}'_{\mathrm{p}} = \begin{pmatrix} \varepsilon'_{\perp} & 0 & 0 \\ 0 & \varepsilon'_{\perp} & 0 \\ 0 & 0 & \varepsilon'_{\parallel} \end{pmatrix}, \tag{1}$$

where $\varepsilon'_{\perp}$ and $\varepsilon'_{\parallel}$ are the dielectric permittivity of ice when the electrical field vector is perpendicular and parallel to the c axis, respectively. In other words, the dielectric permittivity of ice has uniaxial symmetry. In frequency ranges used for radar sounding, $\varepsilon'_{\perp}$ and $\varepsilon'_{\parallel}$ increase from about 3.15 to 3.19 and from about 3.12 to 3.16, respectively, as ice temperature increases from –60°C to 0°C (e.g. Fujita and others, 2000). Dielectric permittivity is, in principle, a complex number but here we utilize only the real part, ε'. We will later discuss how to handle the imaginary part. The dielectric anisotropy $\Delta\varepsilon'$ is given by

$$\Delta\varepsilon' = \varepsilon'_{\perp} - \varepsilon'_{\parallel}. \tag{2}$$

Matsuoka and others (1997) gave precise values of dielectric anisotropy at 30–39 GHz as a function of temperature in the range 194–253K as

$$\Delta\varepsilon'(T) = 0.0256(\pm 0.00137) + 3.57 \times 10^{-5}\left(\pm 6.0 \times 10^{-6}\right)T, \tag{3}$$

where T is the absolute temperature.

Because $\Delta\varepsilon'$ is more than 1% of the ice permittivity, the ice is birefringent for vertically propagated radio waves, as long as the COF is neither a perfect vertical single pole nor perfectly random. Radio waves can propagate within the birefringent ice only with an electrical field along the two principal axes of the dielectric permittivity tensor. Using this physical principle, some algorithms of radar soundings have been suggested to determine the principal axes of the COF and the degree of anisotropy (e.g. Hargreaves, 1977; Doake, 1981). However, there are many other conditions that can be studied to extract COF information from radar-sounding data.

The earlier theories and algorithms for the radio-wave birefringence are from solutions of Maxwell's equation. As an ice sheet is composed of layers of differing permittivity and birefringence, which can be approximately described as a layered medium, practical formulas need to be both easily

https://doi.org/10.3189/172756506781828548 Published online by Cambridge University Press

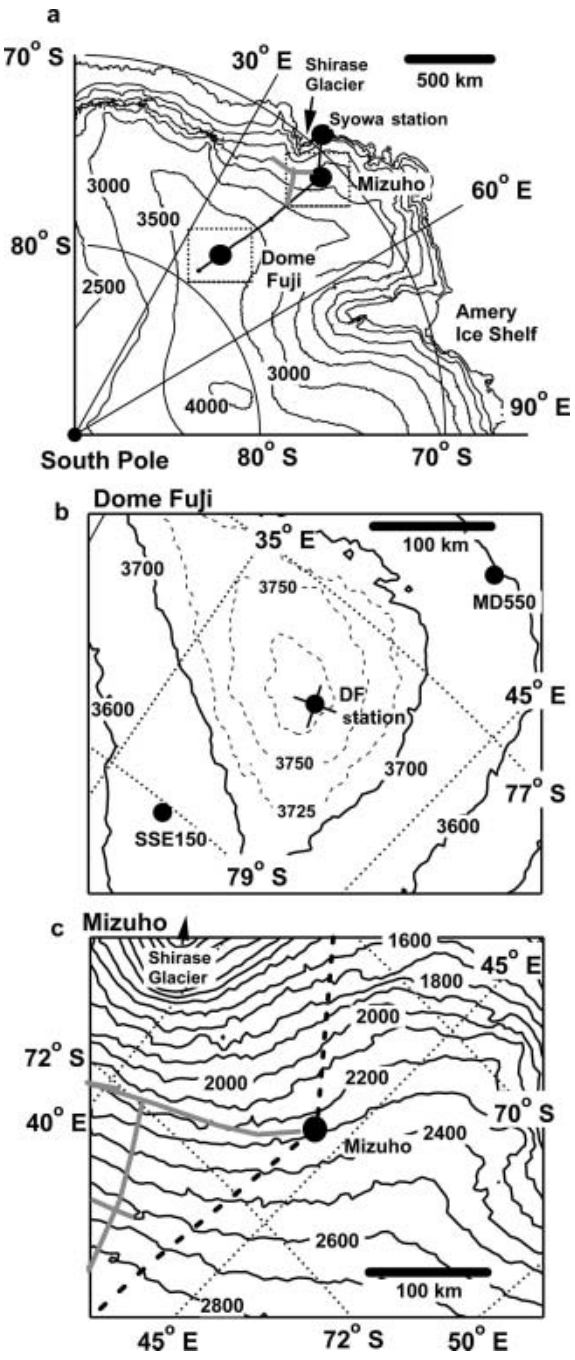

Fig. 1. Topographic maps of East Antarctica. Surface elevation data are from the ERS-1 (European Remote-sensing Satellite-1) high-resolution map of Antarctica compiled by Rémy and others (1999). (a) The solid thick line is the path of a 1150 km long traverse route from the summit region of Dome Fuji, through Mizuho station, to Syowa station (Fujita and others, 1999). The gray thick lines are traverse routes by Matsuoka and others (2003). The map covers about 2500 × 2500 km including east Dronning Maud Land. The dotted squares around Dome Fuji and Mizuho are enlarged in (b) and (c). (b) Enlarged map around Dome Fuji (DF). The cross lines at the station mark the principal axes of COF deduced from this study. (c) Enlarged map at Mizuho. The gray thick lines and a dashed line are traverse routes by Matsuoka and others (2003) and Fujita and others (1999, 2002), respectively.

expandable and flexible to a layering structure. For this reason, we adopt a matrix-based approach, as known for instance from geometrical optics, to implement radio-propagation properties into our model. As for earlier radargram studies, modeling algorithms employed several approaches, based on simple convolution of a source wavelet with medium properties (Moore, 1988; Miners and others, 1997; Kohler and others, 2003) or numerical expression of Maxwell's equations (Kanagaratnam and others, 2001; Miners and others, 2002; Eisen and others; 2003; Arcone and others, 2005). None of these approaches incorporated the anisotropic physical properties of ice.

In addition, modern knowledge of the radio-wave backscatter from within ice needs to be included in the theory. To receive a radar echo, the signal must be backscattered. Sudden or gradual changes of dielectric permittivity and conductivity between ice layers can cause scattering. Layers of differing permittivity arising from differences of density and COF, and changes of conductivity caused by changes of acidity, hereafter P_D, P_{COF} and C_A, respectively, are used as the major causes of scattering within ice. This interpretation means that the return signal depends on the scattering mechanism. For example, if COF patterns are anisotropic in the horizontal plane, radio-wave scattering can be anisotropic. Another example is that, depending on types of scattering, both amplitude and phase delay are highly different at the scattering boundary (e.g. Fujita and others, 2000). These phenomena significantly affect the return signal interpretation. Thus, investigation of the polarization state of radio waves requires examination not only of birefringence but also of the nature of scattering. P_{COF}-based anisotropic scattering can occur where lateral ice strain is significant (Fujita and others, 2003; Matsuoka and others, 2003, 2004); but the other two scattering mechanisms are normally interpreted as being isotropic. Since the primary source of scattering can differ in polar ice depending on depth and physical condition (e.g. Fujita and others, 1999; Matsuoka and others, 2003), we need a model that incorporates such scattering mechanisms, anisotropy in particular.

In this paper, we first present a matrix-based radio-wave propagation model to study the two-way travel of depolarized radio waves within birefringent ice. The model can treat multiple anisotropic and isotropic scattering interfaces, and it can easily incorporate permittivity and conductivity profiles along ice cores into a synthesized radargram. We apply the model to a few ideal cases and demonstrate how both birefringence and COF-based anisotropic scattering can affect the propagation of radio waves in real ice sheets. We also examine how several radar frequencies can be used to fully exploit the potential of the method for extracting COF information from an ice sheet and to distinguish permittivity-based reflections from conductivity-based reflections.

Second, we apply this method to a recent field experiment. We test the theory using data from a polarized, two-frequency radar system at two different inland sites in Antarctica. The COF has already been measured from ice cores at these two sites so they provide the opportunity to examine how radar echoes are related to COF in real ice sheets. One site is Dome Fuji (77°19′ S, 39°40′ E; 3810 m a.s.l., ice thickness 3028 ± 15 m) located near a dome summit. The other is Mizuho (70°42′ S, 44°17′ E; 2250 m a.s.l.; ice thickness 1950 ± 15 m), located in a zone of convergent ice flow (Fig. 1). The radar measurements were carried out between 1995 and 1997 as a series of experiments previously described by Fujita and others (1999, 2002, 2003).

https://doi.org/10.3189/172756506781828548 Published online by Cambridge University Press

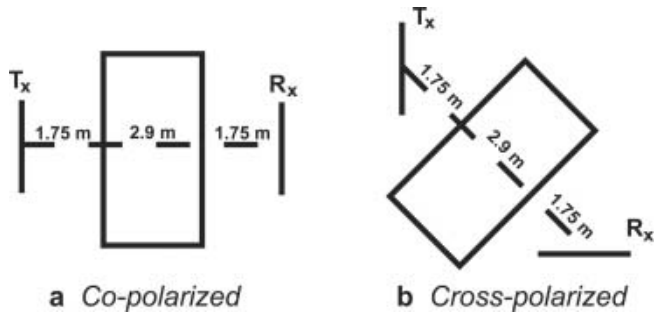

Fig. 2. Top views of antenna arrangements for (a) co-polarization and (b) cross-polarization measurements. For both arrangements, the transmitting (T_x) and receiving (R_x) antennae are at opposite sides of the snow vehicle (shown as a rectangle). The centers of the three-element Yagi antennae are 3.2 m above the ice-sheet surface.

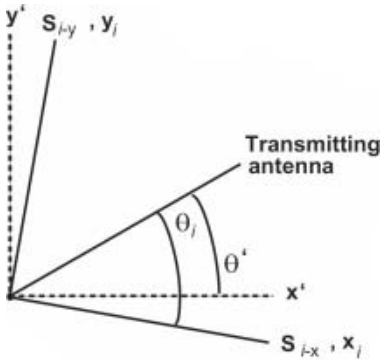

Fig. 3. Coordinate systems used in the theory. The polarization of the transmitting antenna is along the line shown. The principal axes of birefringence at layer i are along x_i and y_i, which are the same as the principal axes of the scattering surface S_{i-x} and S_{i-y}, whereas the measurement frame is x' and y'. The receiving antenna orientation (not shown) is either parallel to the transmitting antenna, for the co-polarized measurements, or perpendicular to the transmitting antenna, for the cross-polarized measurements. Results of simulations are obtained for the case where the principal axes of birefringence and the scattering boundary are consistent with each other at any given depth.

In this paper, we find that data at Dome Fuji are dominated by typical features resulting from birefringence. We verify that the observed radio-wave propagation patterns are explained by orientation and structure of the COF and we determine both strength and orientation of birefringence at Dome Fuji. In contrast, the radar data at Mizuho are affected by both birefringence and anisotropic scattering. We argue that radar methods can be used to determine principal axes and strength of birefringence of the ice sheets. The example at Mizuho shows that in some conditions the radar method applies to the determination of principal axes and strength of anisotropic scattering caused by COF, but not to the strength of birefringence. We then discuss the ability of the radar method to detect dynamic ice-sheet conditions.

2. A MATRIX-BASED RADIO-WAVE PROPAGATION MODEL

2.1. Description of the model

Radar polarimetry uses matrix-based formulas to describe transmission and scattering processes (e.g. Ulaby and Elachi, 1990; Stutzman, 1992). The use of a matrix approach has two advantages. First, transmission through each layer and scattering at each layer boundary are described with a matrix that can be determined from ice cores. Second, the computations can handle an arbitrary number of layers, each layer with its own principal axes.

We model the propagation of radio waves traveling along the near-vertical. The modeled processes include transmission at the ice-sheet surface, scattering within the ice and the returning transmission within the ice. We assume that the ice sheet is comprised of a number of layers, N, each labeled i, with deeper layers having larger i values. Each layer has a transmission matrix $\mathbf{T}_i$ to describe the transmission in layer i, and a scattering matrix $\mathbf{S}_i$ to describe the backscattering at the boundary between layer i and layer $(i+1)$. These matrices are described below.

We refer to the backscattering process of radio waves in the ice sheet using the term 'scattering'. In general, scattering refers to any re-emission of waves. However, it is commonly thought that, for ice sheets, scattering sources of radio waves are distributed as if from stacked layers in the ice sheet. We could have used the term 'reflection' instead of 'scattering', as we describe the macroscopic properties and neglect microscopic properties such as surface roughness or individual scatterers. Despite our simplifications, we keep the term 'scattering' for consistency with our implementation of a scattering matrix.

Polarimetric radar measurements

We model two radar configurations, each using linearly polarized antennae for transmitting and receiving. A 'co-polarized' configuration is one in which the transmitting antenna is parallel to the receiving antenna, while a 'cross-polarized' configuration is one in which the antennae are perpendicular. Figure 2 shows how we measure the orthogonal components of the macroscopic electrical field vector parallel and orthogonal to the transmitting antenna. In the field, the transmitter and receiver antenna are set up parallel to and orthogonal to each other for the two different configurations.

Figure 3 shows the coordinate systems for the radar antennae and for the principal axes in ice. The orthogonal coordinate system (x', y', z') is set so that the z' axis is vertical (positive downward), but the horizontal axes x' and y' can be defined arbitrarily. For example, they can be defined by an observer in the field to be along the flowline, transverse line or in some geographical direction. When we rotate antennae in the horizontal plane, θ' is the angle of the transmitting antenna counterclockwise from x'. Within ice, the transmission matrix $\mathbf{T}_i$ and scattering matrix $\mathbf{S}_i$ have common principal axes within each layer because in principle COF produces both depolarization and anisotropic scattering. We define the axes x_i and y_i as the common principal axes of matrices $\mathbf{T}_i$ and $\mathbf{S}_i$ at the ith layer and θ_i as the angle of the transmitting antenna counterclockwise from one of the common principal axes, x_i. Therefore, we simplify the model by assuming that the P_{COF} mechanism dominates the anisotropy and the P_D and C_A mechanisms cause only isotropic scattering.

The model calculates the orthogonal components of the macroscopic electrical field vector parallel (P) to and

https://doi.org/10.3189/172756506781828548 Published online by Cambridge University Press

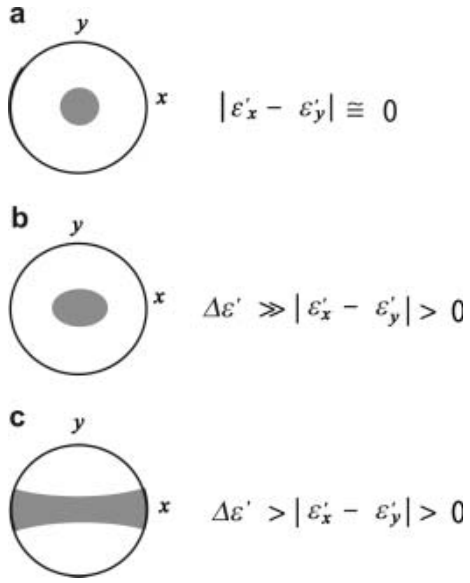

Fig. 4. Schmidt diagrams show typical COFs in inland ice cores (e.g. Fujita and others, 1987; Lipenkov and others, 1989; Azuma and others, 2000). The vertical direction is normal to the plane of the paper and at the center of the diagram. The relative magnitudes of dielectric permittivity tensor elements (ε'_x and ε'_y) in the horizontal plane are given at the right of each diagram. (a) A perfect circular single-pole COF. If the cluster of the *c* axes does not have any deviations, the dielectric permittivity tensor elements in all orientations in the horizontal are the same and no birefringence can occur. (b) An elongated single-pole COF. There is significant birefringence in the horizontal plane, but inhomogeneity of the dielectric permittivity components is much smaller than the dielectric anisotropy of single crystals $\Delta\varepsilon' = 0.034$ (Matsuoka and others, 1997). (c) Vertical girdle-type COF. The dielectric anisotropy can be much larger than in (b). Thus birefringence should have a strong effect.

orthogonal (O) to the transmitting antenna. They are written as follows:

$\begin{pmatrix} E_{PT} \\ E_{OT} \end{pmatrix}$: transmitted electrical field at the antenna ($E_{PT} \gg E_{OT}$)

$\begin{pmatrix} E_P \\ E_O \end{pmatrix}_i$: electrical field incident to the scattering boundaries at the *i*th layer

$\begin{pmatrix} E'_P \\ E'_O \end{pmatrix}_i$: electrical field scattered from scattering boundaries at the *i*th layer

$\begin{pmatrix} E_{PR} \\ E_{OR} \end{pmatrix}$: electrical field received at the antenna

Here, the macroscopic field means the field averaged over a volume that is much larger than each ice crystal (~mm) but significantly smaller than the radar wavelength (~m or longer).

Dielectric permittivity tensor and electrical conductivity tensor

The relative complex dielectric permittivity is generally expressed as:

$$\varepsilon^* = \varepsilon' - j\varepsilon'' \quad \left(j = \sqrt{-1}\right),$$

where ε' and ε'' are the real and imaginary parts, respectively. Electrical conductivity is related to the imaginary part of the permittivity as:

$$\sigma = \omega\varepsilon_0\varepsilon'',$$

where ε_0 is the dielectric permittivity in a vacuum and ω is the angular frequency. We express ice properties using only the real part of the relative permittivity, ε', and electrical conductivity, σ.

The elements in $\mathbf{T}_i$ and $\mathbf{S}_i$ depend on the dielectric permittivity tensor of the layer. When the COF is symmetric around the vertical, as is typical of inland ice sheets (e.g. Fig. 4), the dielectric permittivity of ice has two principal axes in the horizontal plane, thus:

$$\boldsymbol{\varepsilon}'_i = \begin{pmatrix} \varepsilon'_{i-x} & 0 & 0 \\ 0 & \varepsilon'_{i-y} & 0 \\ 0 & 0 & \varepsilon'_{i-z} \end{pmatrix}, \tag{4}$$

where ε'_{i-x} and ε'_{i-y} are in the horizontal plane and ε'_{i-z} is along the vertical. The subscript *i* denotes the *i*th layer and all three components are real numbers. However, the orientation of the two principal axes in the horizontal plane can vary with both location and depth. We also use the electrical conductivity to determine absorption of the radar waves. Like the permittivity, absorption is written as a diagonal matrix, but with elements σ_{i-x}, σ_{i-y} and σ_{i-z}. Each component of the tensors $\boldsymbol{\varepsilon}'_i$ or σ_i is an average over the *i*th layer. The dielectric permittivity tensor can be obtained either by direct measurements of the anisotropic permittivity of the ice core (e.g. Matsuoka and others, 1998) or by calculations from ice-core COF data (see Appendix). The electrical conductivity can be determined from ice cores by ECM (electrical conductivity method) or DEP (dielectric profiling). Matsuoka and others (1997) and Fujita and others (2000) found that the electrical conductivity in pure single crystals of ice has uniaxial symmetry at radar wavelengths. However, the electrical conductivity in acidic polar ice is much larger than that of pure single crystals. In Antarctica, electrical conductivity is typically of the order of 10^{-5} S m^{-1}. Measurements have so far found no significant anisotropy of electrical conductivity in the typically acidic, polycrystalline ice of the polar regions. Therefore, we assume σ_{i-x} is approximately as large as σ_{i-y}. Moreover, electrical conductivity is independent of frequency at frequencies below about 600 MHz, within the temperature range of the polar ice sheets (e.g. Moore and Fujita, 1993; Fujita and others, 2000).

Transmission and scattering matrices

The transmission matrix, $\mathbf{T}_i$, describes the transmission of radio waves through birefringent ice. In the reference frame of the principal orientations, $\mathbf{T}_i$ is defined as:

$$\mathbf{T}_i = \begin{pmatrix} T_{i-x} & 0 \\ 0 & T_{i-y} \end{pmatrix}. \tag{5}$$

$\mathbf{T}_i$ describes changes of both phase and amplitude of the waves along these two orientations, compared with the same waves propagating in a vacuum. The two components are

$$T_{i-x} = \exp\left(-jk_0\Delta z_i + jk_{i-x}\Delta z_i\right), \tag{6a}$$
$$T_{i-y} = \exp\left(-jk_0\Delta z_i + jk_{i-y}\Delta z_i\right), \tag{6b}$$

where $k_0 = 2\pi/\lambda_0$ (rad m^{-1}) is the wavenumber in a vacuum, with λ_0 the wavelength in a vacuum, k_{i-x} and k_{i-y} are the propagation constants along the two principal axes for the *i*th layer and Δz_i is the thickness of the *i*th layer. Both k_{i-x} and k_{i-y} can be expressed as functions of dielectric

https://doi.org/10.3189/172756506781828548 Published online by Cambridge University Press

Table 1. Characteristics of three major radar scattering mechanisms within ice sheets

	P_D	P_{COF}	C_A
Electrical property that causes scattering	permittivity	permittivity	conductivity
Physical cause of scattering	density fluctuation	crystal-orientation fabrics	strong acids*
Type of scattering	isotropic†	anisotropic	isotropic†
Dependence on frequency	independent	independent	inversely proportional
Effect of temperature	weak	weak	strong

*Strong acids that cause conductivity changes are from volcanic aerosols. Volcanic dust layers typically do not form highly acidic layers in the Antarctic ice sheet.
†Possible exceptions are discussed in the text.

permittivity and electrical conductivity. Maxwell's equations give

$$k_{i-x} = \left(\varepsilon_0\mu_0\varepsilon'_{i-x}\omega^2 + j\mu_0\sigma_{i-x}\omega\right)^{0.5}, \quad (7a)$$

$$k_{i-y} = \left(\varepsilon_0\mu_0\varepsilon'_{i-y}\omega^2 + j\mu_0\sigma_{i-y}\omega\right)^{0.5}, \quad (7b)$$

where μ_0 is the magnetic permeability in a vacuum.

The scattering matrix $\mathbf{S}_i$ has two principal components:

$$\mathbf{S}_i = \begin{pmatrix} S_{i-x} & 0 \\ 0 & S_{i-y} \end{pmatrix}. \quad (8)$$

Like the transmission matrix, $\mathbf{S}_i$ is determined from the dielectric permittivity and electrical conductivity of the ice layer. When the scattering is isotropic, $S_{i-x} = S_{i-y}$. When the scattering is anisotropic, one of these two components is significantly larger than the other. The elements of the complex scattering matrix are known as 'complex scattering amplitudes' (Ulaby and Elachi, 1990). When the scattering at layer interfaces is approximated by reflection, the components of $\mathbf{S}_i$ are the complex amplitude reflection coefficients described, for example, in Ackley and Keliher (1979), Moore (1988) and Fujita and others (2000).

Each of the three major scattering mechanisms (P_D, C_A and P_{COF}), has its own distinctive properties. The dominance of one mechanism over the others depends on conditions such as the depth range of the ice, position along the ice flowline, strain history, temperature, depositional environment and radar frequency. These conditions and properties are summarized in Table 1. If one of these three mechanisms is particularly strong, then that mechanism can be inferred from the radar data. However, when the dominant scattering mechanism is P_{COF} but the other scattering mechanisms have only slightly weaker scattering amplitudes the data can be difficult to interpret. This is because the effect of P_{COF} appears in one orientation but the effects of the other mechanisms can appear in the orthogonal orientation. In such cases, the handling of both amplitude and phase is complicated due to the waves along two principal axes scattering by different mechanisms. Although this matrix-based model can handle such complicated cases, we assume here that one scattering cause is dominant for all radar polarizations.

Electrical field along the propagation path

The propagation of radio waves from the transmission antenna towards the scattering boundary at depth z can be represented by

$$\begin{pmatrix} E_P \\ E_O \end{pmatrix}_N = \frac{\exp(jk_0 z)}{4\pi z} \prod_{i=1}^{N} [\mathbf{R}(\theta_i)\mathbf{T}_i\mathbf{R}(-\theta_i)] \begin{pmatrix} E_{PT} \\ E_{OT} \end{pmatrix}, \quad (9)$$

where $\mathbf{R}(\theta_i)$ is the rotation matrix that accounts for the azimuthal shift of principal axes measured from the transmitting antenna (Fig. 2)

$$\mathbf{R}(\theta_i) = \begin{pmatrix} \cos\theta_i & -\sin\theta_i \\ \sin\theta_i & \cos\theta_i \end{pmatrix}. \quad (10)$$

Equation (9) expresses the propagation through all layers to the Nth layer. The equation is composed of (i) free space propagation, (ii) summation of changes of both phase and amplitude of the waves as compared with the same waves propagating in a vacuum and (iii) incident field. The expression allows one to calculate any depth sequence of azimuthal orientations of the principal axes. In the simplest case in which the principal axes have the same azimuthal angle over the full ice thickness, the principal axes of $\mathbf{T}_i$ are the same at all depths, which simplifies the calculation. Scattering at a boundary between the ith and $(i + 1)$th layer is described through

$$\begin{pmatrix} E'_P \\ E'_O \end{pmatrix}_i = \mathbf{R}(\theta_i)\mathbf{S}_i\mathbf{R}(-\theta_i) \begin{pmatrix} E_P \\ E_O \end{pmatrix}_i. \quad (11)$$

Radar echoes for pulse-modulated radars are the sum of scattering events within the depth range defined as that depth in which the radio wave travels for a half of the pulse width. The upward propagation of the scattered radio wave is opposite to the downward propagation described by Equation (9). In particular,

$$\begin{pmatrix} E_{PR} \\ E_{OR} \end{pmatrix} = \frac{\exp(jk_0 z)}{4\pi z} \prod_{i=1}^{N} [\mathbf{R}(\theta_{N+1-i})\mathbf{T}_{N+1-i}\,\mathbf{R}(-\theta_{N+1-i})] \begin{pmatrix} E'_P \\ E'_O \end{pmatrix}_N. \quad (12)$$

These equations are consistent with the radar equations (e.g. Ulaby and others, 1981), but do not include radar system characteristics such as antenna gain and the effective area of scattering.

If we consider the complex dielectric permittivity tensor of each layer in the ice sheet and synthesize the primary reflection components from each boundary, we can calculate synthetic radargrams. For such a calculation, one needs ice-core data, and the sampling rate of the data in ice needs to be much finer than the wavelength in ice. We do not consider multiple scattering because it is negligible. This is consistent with estimates based on the dielectric properties of ice; in particular, the scattering coefficients are below about –40 dB for shallow ice with the P_D mechanism and below about –60 dB for deeper ice with the P_D, C_A and P_{COF} mechanisms (Fujita and others, 2000). This is consistent with the radargram simulations of Miners and others (2002) in which effects from the secondary and further reflections

https://doi.org/10.3189/172756506781828548 Published online by Cambridge University Press

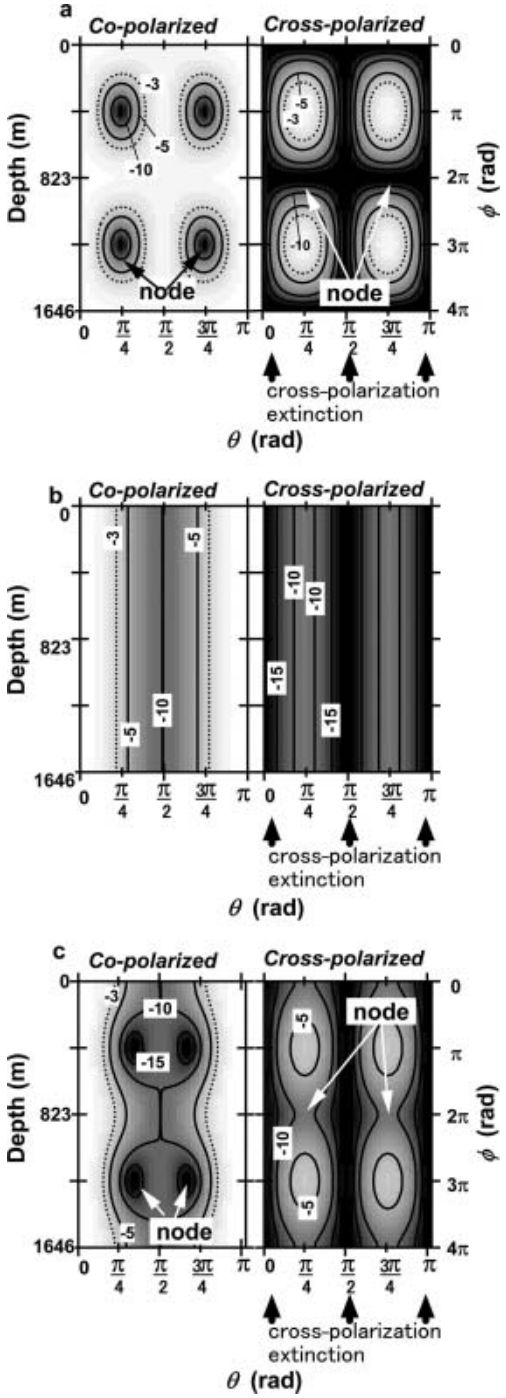

Fig. 5. Received power intensity from an echo sounding in ice relative to that of a wave within an isotropic medium and scattered off isotropic boundaries. The co-polarized case is on the left and the cross-polarized case is on the right of each panel. Results are shown as a function of ice depth (left axis) or phase difference between waves along two principal axes at the receiving antenna (ϕ, right axis), and the antenna orientation measured from x (θ, bottom axis; $\theta = 0$ is parallel to the principal axes). Abscissa values from π to 2π are the same as those from 0 to π. The radar frequency is 179 MHz. (a) Birefringent ice sheet with isotropic scattering boundaries. The anisotropy in the dielectric permittivity tensor is $0.1\Delta\varepsilon'$ or 0.0034. (b) Ice sheet without birefringence but with 10 dB anisotropic scattering boundaries. (ϕ is not shown for this case because there is no birefringence.) (c) Birefringent ice sheet as in (a) with 10 dB anisotropic scattering boundaries.

were negligibly small. Also, we note that there are several factors that may exist in reality but are not considered in the present matrix modeling. They are, for example, (i) spatial lateral variation of the COF, (ii) non-planar reflection surfaces and (iii) side lobe effects of the radar system. In both the real ice sheet and specification of the radar system these are significantly different from the idealized situations considered in our model; these factors may contribute to the model results.

2.2. Model results

To test the model, we simulated three cases. The first assumes the birefringence effect only, the second assumes only anisotropic scattering and the third assumes a combination of birefringence and anisotropic scattering. These three cases are idealized, but they represent common features in Antarctica (Matsuoka and others, 2003). To focus on the polarimetric features, we do not consider isotropic effects including geometrical spreading, dielectric absorption due to electrical conductivity or effective area for scattering, though they do not add any difficulty to the theory. We examine variations in the echo in terms of radar frequency and polarization. To extract effects of birefringence and anisotropic scattering boundaries, we focus on both phase and amplitude anisotropy in the electric field from Equations (9–12).

Isotropic scattering with birefringence

Figure 5a shows how birefringence affects the received power profiles. In the calculation, we set $\varepsilon'_{i-x} = \varepsilon'_{i-y} - 0.1\Delta\varepsilon'$, and assume isotropic reflection (i.e. $S_{i-x} = S_{i-y}$). We assume scattering occurs everywhere and that the same mechanism causes reflections in both components S_{i-x} and S_{i-y}. We set a discrete number of layers, 600, in the model. Here, 'the same mechanism' means that the mechanism can be either P_D, P_{COF} or C_A. Whatever the mechanism is, as long as a single mechanism works, it does not change the results of the simulations. We do not consider cases where two or more mechanisms are mixed in a single ice column. For the two-way travel to a point z_1, phase difference between waves along the two principal axes occurs. Phase difference, ϕ, is

$$\phi = \frac{4\pi f}{c}\int_{z_1}^{0}\left(\sqrt{\varepsilon'_x} - \sqrt{\varepsilon'_y}\right)\mathrm{d}z + \left(\Delta\phi_x - \Delta\phi_y\right), \qquad (13)$$

where f is the frequency used for radar sounding and c is the speed of light in a vacuum. The square root of the dielectric permittivity is equivalent to the refractive index of ice. The second term is the phase shift at the scattering boundary at z_1. In our simulations, we assume $\Delta\phi_x = \Delta\phi_y$. All simulations are carried out at a single frequency of 179 MHz, the same frequency as used in our radar experiments in the field. But differences in frequency affect the relation between ϕ and z in Equation (13). In terms of the results of the modeling, effects from ϕ are important.

Features of the simulated results are as follows. For the co-polarized simulation (left panel of Fig. 5a), the echo intensity decreases at two antenna azimuths ($\theta = \pi/4$ and $3\pi/4$) when the phase difference, ϕ, between waves along two principal axes becomes an odd multiple of π. Hereafter, we call this feature a 'co-polarization node'. For the cross-polarized simulation (right panel of Fig. 5a), extinction of the signal appears at every $\pi/2$ of the antenna rotation angle, θ.

https://doi.org/10.3189/172756506781828548 Published online by Cambridge University Press

Here, θ is the angle from one of the two principal axes, that is, θ_i is the same for all i. Such an extinction of the signal is known in optical measurements of thin ice sections between crossed polarizers. Hereafter, we call this feature 'cross-polarization extinction'. We also note, for the cross-polarized simulation, a decrease of the signal level appears at every 2π of ϕ at the antenna azimuths, $\theta = \pi/4$ and $3\pi/4$. Hereafter we call this feature the 'cross-polarization node'.

Anisotropic scattering with no birefringence

Figure 5b shows a simulated result for anisotropic scattering boundaries, but with no birefringence. Here, we assume $S_{i-x} = 10S_{i-y}$ In real ice sheets anisotropic scattering boundaries are caused by anisotropic COF. Thus, anisotropic scattering boundaries typically occur *with* some amount of birefringence. Cases like Figure 5b occur when the birefringence is very weak compared with the effect of anisotropic scattering. We note that there are no observed examples of anisotropic scattering boundaries caused by P_D or C_A in the literature. In the simulation, we again assume that the same mechanism causes reflections in both components S_{i-x} and S_{i-y}, so that no relative phase difference occurs between the two components at the scattering boundary, $\Delta\phi_x = \Delta\phi_y$ in Equation (13). One can see that for the co-polarization antenna configuration, the received power depends only on θ, with a periodicity of π. For the cross-polarization configuration, cross-polarization extinction occurs just as it did in the case of birefringent ice. Thus, this cross-polarization extinction is common to both the birefringent case and anisotropic scattering.

Anisotropic scattering with birefringence

Figure 5c shows the simulated results for a birefringent ice sheet containing anisotropic boundaries. We merge the above cases $\varepsilon'_{i-x} = \varepsilon'_{i-y} - 0.1\Delta\varepsilon'$ (Fig. 5a) and $S_{i-x} = 10S_{i-y}$ (Fig. 5b). We assume that the same mechanism causes reflections in both components S_{i-x} and S_{i-y}, so no relative phase difference occurs between the two components at the scattering boundary. We further assume that both birefringence and anisotropic boundaries have the same principal axes. Such a situation can occur (i) when the cluster strength of the elongated vertical single-pole COF changes with depth, (ii) when the cluster strength of the vertical girdle-type fabric changes with depth (e.g. Fujita and others, 2003) and (iii) when vertical single-pole COF layers are intermingled with vertical girdle-type fabric layers (e.g. Lipenkov and others, 1998; Fujita and others, 2003; Matsuoka and others, 2003, 2004). Features of the signal patterns are summarized as follows. The co-polarization signal node shifted closer to the weaker axis ($\theta = \pi/2$) of the scattering. This is because we biased the amplitude, by 10 dB, of the wave on one principal axis over the other, in order to simulate the effect of anisotropic boundaries. For the same reason, in the cross-polarized configuration, even with θ around $\pi/4$ and $3\pi/4$ and with ϕ around $2n\pi$ ($n = 1,2,\ldots$) waves along the two principal axes do not cancel each other out. This effect makes the cross-polarization node weaker than that in the pure birefringence case (Fig. 5a). For the cross-polarization case, extinction occurs at the same azimuths as those in Figure 5a and b. We note here that the spreading of the radar beam will not affect the results because the beam from the nadir is the strongest.

In summary, Figure 5a shows a previously studied birefringent effect (e.g. Hargreaves, 1977), but we have reproduced it using matrix-based modeling. Figure 5b and c show new cases that could not be shown from earlier studies of the isotropic scattering mechanisms, P_D and C_A (Fujita and others, 2000, 2003; Matsuoka and others, 2003). The results in Figure 5b and c require P_{COF} to be one of the dominant scattering mechanisms in the ice sheet. In addition, in the light of the present knowledge of $\Delta\varepsilon'$, we derive quantitative relationships between depth, phase difference, radar frequency and COF features.

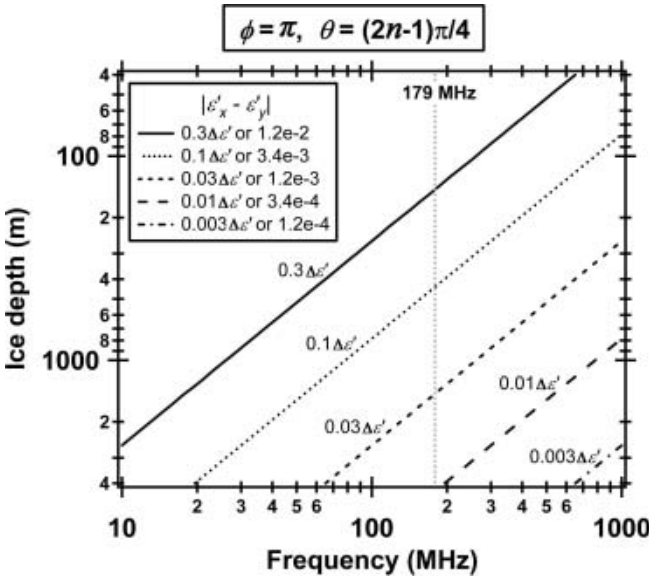

Fig. 6. Depths at which the shallowest co-polarized node ($\phi = \pi$) occurs are shown in terms of the radar frequency and the COF dielectric anisotropy. $\Delta\varepsilon'$ is the dielectric anisotropy of pure-ice single crystals. The vertical line at 179 MHz indicates the radar frequency used in our simulations and in observations.

2.3. Implications for radar surveys

Depth of the shallowest co-polarized node

The simulated results in Figure 5 indicate that the birefringent effect will usually appear as a node in experimental conditions in which the radar return has a ϕ value that is close to an integer multiple of π. As this is a point that should be readily detectable, we focus on these nodes. By setting $\phi = \pi$ in Equation (13) we find the resulting depth values for various frequencies, f, and COF anisotropies. Figure 6 shows how ϕ reaches π as a function of the strength of the COF anisotropy and the radar frequency. In the graph, the abscissa is the frequency range used for radar sounding and the ordinate is the depth range of polar ice sheets. The lines in Figure 6 show the depths for the shallowest co-polarized node ($\phi = \pi$) in terms of dielectric anisotropy of the ice-sheet ice. Values of dielectric anisotropy below about $0.3\Delta\varepsilon'$ can occur in ice sheets when the COF is a vertical girdle pattern (e.g. fig. 4 in Fujita and Mae, 1993). Also, values below about $0.1\Delta\varepsilon'$ are expected when the COF is an elongated vertical single pole. Thus, Figure 6 suggests that the co-polarized nodes should be observable in a radar sounding. When the radar frequency is higher or the COF anisotropy is stronger, the signal nodes appear at shallower depths. A higher-frequency radar makes it possible to detect co-polarized nodes caused by the weaker ice-crystal anisotropy.

https://doi.org/10.3189/172756506781828548 Published online by Cambridge University Press

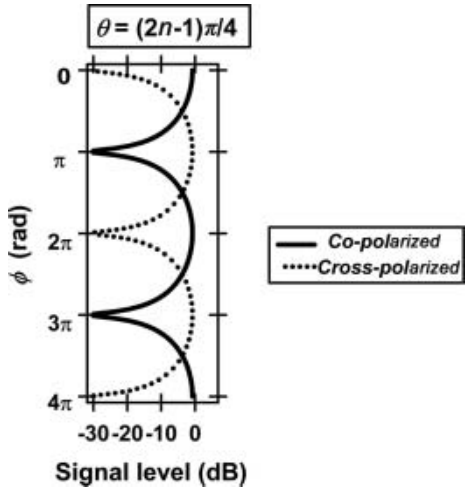

Fig. 7. Relative intensity of the returned radar signal along orientation $\theta = (2n - 1)\pi/4$, based on Figure 5a. Both co-polarized and cross-polarized cases are shown.

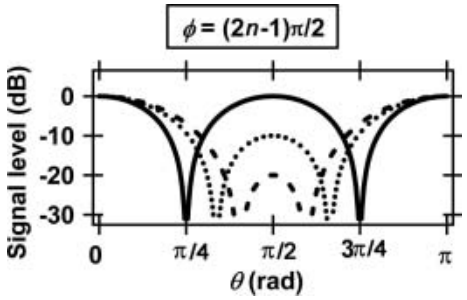

Fig. 8. Relative intensity of the returned radar signal along phase difference $\phi = (2n - 1)\pi/2$ for ice with birefringence and anisotropic scattering level, based on the co-polarized data cross-section in Figure 5c. The magnitudes of anisotropy are: 0 dB, solid line; –10 dB, dotted line; –20 dB, dashed line.

Extracting anisotropy in COF

The above results for the co-polarization configuration suggest that we can extract COF information from the radar-sounding data. The same analysis can be applied to the cross-polarization node and extinction. The most distinct features include the co-polarization nodes, the cross-polarization extinction and the cross-polarization node, as we saw in Figure 5. By finding these features in field data, one can determine the COF anisotropy, the orientation for the COF anisotropy and the depths where $\phi = n\pi$.

An example of this approach is shown in Figure 7 in which the received power is shown to vary with ϕ. The feature of interest here is the cusps in the signal. Using such a plot and Equation (13) one can determine the depth-averaged magnitude of $\left|\sqrt{\varepsilon'_x} - \sqrt{\varepsilon'_y}\right|$ between depths of the cusps. This has been done for two sites in Antarctica and is presented below. In addition, because ϕ is proportional to the radar frequency, use of a multi-frequency radar system allows us to determine the magnitude of $\left|\sqrt{\varepsilon'_x} - \sqrt{\varepsilon'_y}\right|$ at many depth ranges. The higher the frequency, the larger the number of features or the shorter the depth interval between the features. Both the magnitude of the birefringence and the directions of the principal axes are useful for understanding the strain history within ice over a wide area.

Effects from anisotropic scattering

When both anisotropic scattering and birefringence affect the signal significantly, the model shows that the antenna azimuth of the co-polarization nodes moves from $\pi/4$ toward the azimuth $\theta = \pi/2$ at which the weakest scattering occurs as the scattering anisotropy gets larger. Figure 8 shows how the co-polarization node shifts at a fixed depth when the anisotropy changes from 0 to –20 dB. At the same time, the signal near $\theta = \pi/2$ gets weaker. This shift of the azimuthal angle of the node is nearly proportional to the anisotropy in decibels. We fit the relation to 0.024 rad dB^{-1} (1.4° dB^{-1}).

The cross-polarization nodes at $\theta = \pi/4$ and $3\pi/4$ are also weakened by anisotropic scattering. Figure 9 demonstrates how this feature varies in terms of ϕ. When the scattering anisotropy is –10 or –20 dB, the range of signal variations is only about 5 and 2 dB, respectively. Thus, for both the co-polarized and the cross-polarized measurements, the nodes at $\phi = n\pi$ become less distinct when affected by anisotropic scattering. These results suggest that combinations of birefringence and anisotropic scattering make it more difficult to detect co-polarization and cross-polarization nodes than when there is only a birefringent effect.

Table 2 gives a summary of conditions for appearance of co-polarization and cross-polarization signal features. This table is useful when we extract COF information from the radar-sounding data.

Advantages of using several radar frequencies

The amplitude reflection coefficient due to permittivity-based reflections is independent of frequency, whereas the amplitude reflection coefficient due to conductivity-based reflections is inversely proportional to frequency (Table 1). Hence, we can use two frequencies, say f_1 and f_2, to distinguish between the conductivity-based reflections and the permittivity-based reflections. For the co-polarized data, the magnitude of this difference is 20 $\log_{10}(f_2/f_1)$ dB (Fujita and others, 1999). This has been used in several studies taking $f_1 = 179$ MHz and $f_2 = 60$ MHz, resulting in a difference of about 10 dB (Fujita and others, 1999, 2002; Matsuoka and others, 2003).

Doake and others (2002) pointed out a possible case in which the distinctions between permittivity-based reflections (P_D and P_{COF}) and conductivity-based reflections (C_A) are masked by birefringence when the multi-frequency method is used. That is, they claimed that possible fluctuations of the received power due to birefringence could be larger than the 20 $\log_{10}(f_2/f_1)$ dB. The results in Figure 5 suggest an answer to this point. The answer is yes, but the method is still valuable. The reasons are as follows. First, if one knows (i) the principal axes (by scanning θ), (ii) the depths of the co-polarization nodes and (iii) the depths of the cross-polarization nodes, then one can distinguish between effects from birefringence (signal nodes) and effects from the frequency-dependent number, 20 $\log_{10}(f_2/f_1)$ dB. Thus, the polarimetric multi-frequency measurement can distinguish these two effects and provide valuable information on the characteristics within ice sheets.

Second, if neither the principal axes nor the depths of the co-polarization nodes are known, it is more problematic. Our ability to distinguish between permittivity-based reflections and conductivity-based reflections is weakened. Such a situation arises if we use only one arbitrarily selected

https://doi.org/10.3189/172756506781828548 Published online by Cambridge University Press

antenna orientation at a site. However, our simulation suggests the data will still be sufficient to distinguish the scattering mechanisms. In the θ–ϕ diagrams in Figure 5a, the probability of occurrence of signal nodes of 3, 5 and 10 dB are 20%, 12% and 3%, respectively. This probability is defined as the area surrounded by the contour lines relative to the total area of the θ–ϕ diagrams. This means that, when we do not know the principal axes and strength of birefringence at all, the average probability that it will be accidentally affected by birefringence by 10 dB is 3%. However, in ground-based surveys antennae are often set along lines related to ice flow, say parallel or perpendicular to the ice flow direction. Such orientations tend to contain the principal axes of the strain, and thus they would be free from co-polarization nodes. This means that the probability of the two-frequency method being affected accidentally by the co-polarization nodes in a typical ground survey is much smaller than the values given above. But this is only the case for ground-based surveys. Airborne surveys are typically laid out as a grid over larger distances, so co-polarization nodes are more likely to occur.

Finally, the effect is weaker when the radar data are averaged over all θ. In a two-frequency experiment, Fujita and others (1999) and Matsuoka and others (2003) identified the dominant scattering mechanisms at many sites from inland to the coast. They averaged the echo intensity at a given depth over the radar data collected at $\pi/16$ rad or $\pi/8$ rad intervals in the azimuth. Averaging over the azimuth made the node weaker. For example, the effect of the co-polarization node will not exceed 5 dB even in extreme cases.

In summary, our analysis suggests that the best radar-sounding method will include polarimetric radar sounding to distinguish between the effects of birefringence (signal nodes) and effects of frequency. Even if we do not know the directions of the principal axes and the depths of signal nodes, we can distinguish between conductivity-based and permittivity-based reflections. However, the frequencies should not be too close; the value of $20\log_{10}(f_2/f_1)$ should be 10 dB or more, which means that the higher frequency should be at least three times the lower frequency.

Possible effects of pulse width

Radar echoes for pulse-modulated radars are the sum of reflections within the depth range, defined as that in which the radio wave travels the half-distance of the pulse width. The simulated results in Figure 5 do not include effects of pulse width. Rather, Figure 5 shows the radar echo from very short pulses scattered from various depths. For pulse widths between 60 and 1000 ns, which are typically used in ice soundings (e.g. Nixdorf and others 1999; Matsuoka and others, 2003), the depth range is 5–85 m.

This interference does not alter the simulated results, as long as the same interference pattern occurs in the waves along both principal axes. Two complex cases can arise in an ice sheet. First, at the scattering boundaries, the ratio between two components S_{i-x} and S_{i-y} fluctuates from one depth to another. In this case, the interference pattern in waves along the two principal axes is different. Differences get larger as the pulse gets wider. Second, at the scattering boundaries, a relative phase difference can occur between S_{i-x} and S_{i-y}, as we described in section 2.1. If one or both cases occur in an ice sheet, the co-polarization node, the cross-polarization node and the cross-polarization extinction may not appear. It would then be difficult to determine the specific complications which do occur. In the next section we use the results obtained with our matrix model to analyze the presence of birefringence and anisotropic scattering in field radar data.

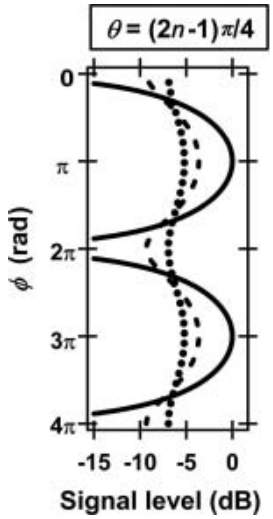

Fig. 9. Relative intensity of the returned radar signal along orientation $\theta = (2n-1)\pi/4$ for ice with birefringence and anisotropic scattering level, based on the cross-polarized data cross-section in Figure 5c. The magnitudes of anisotropy are: 0 dB, solid line; –10 dB, dotted line; –20 dB, dashed line.

Table 2. Conditions for appearance of co-polarization nodes, cross-polarization nodes and cross-polarization extinction

	Co-polarization nodes	Cross-polarization nodes	Cross-polarization extinction
Birefringence	$\theta = (2n-1)\pi/4$ $\phi = (2n-1)\pi$*	$\theta = (2n-1)\pi/4$ $\phi = 2n\pi$	$\theta = n\pi/2$
Anisotropic scattering†	No appearance	No appearance	$\theta = n\pi/2$
Combination of birefringence and anisotropic scattering	$\theta = (4n-3)\pi/4 + 0.024a$‡ $\phi = (2n-1)\pi$ and $\theta = (4n-1)\pi/4 - 0.024a$ $\phi = (2n-1)\pi$	$\theta = (2n-1)\pi/4$ $\phi = 2n\pi$	$\theta = n\pi/2$

*n is a positive integer. ϕ is phase difference between two waves. θ is the angle from one of the two principal axes.
†Signal periodicity along θ is $\pi/2$, in contrast to the birefringence case where it is $\pi/4$.
‡a is the magnitude of the anisotropic scattering expressed in decibels.

https://doi.org/10.3189/172756506781828548 Published online by Cambridge University Press

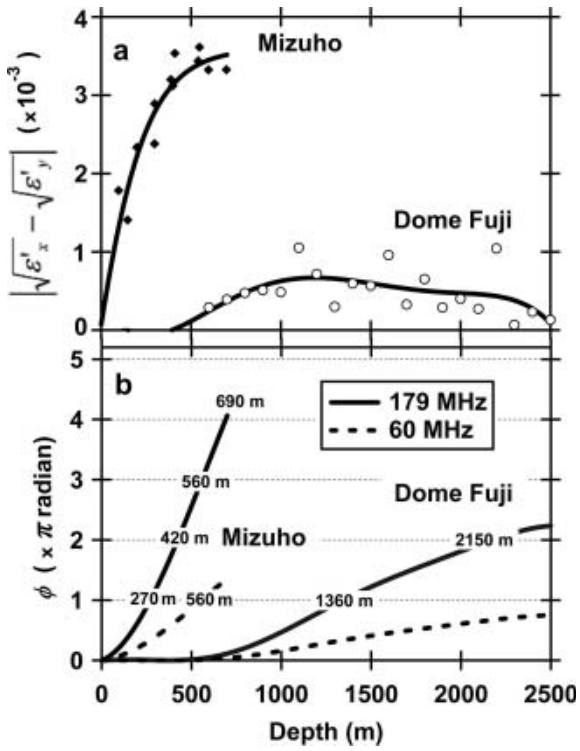

Fig. 10. Depth profiles of horizontal anisotropy in (a) refractive index ($\sqrt{\varepsilon'}$) and (b) radar phase. Each point in (a) represents a set of COF data from a section of ice from ice cores. Open circles indicate the Dome Fuji ice, and solid diamonds indicate the Mizuho ice. Solid lines are fitted curves. (b) The calculated total phase shift, ϕ, during the two-way traveled wave back to the receiving antenna between the components along x and y axes, based on ice-core data according to Equation (13). Depths are given when ϕ is integer multiples of π.

3. RADAR EXPERIMENT

3.1. Location and characteristics of study sites

Dome Fuji

Dome Fuji is the second highest dome summit in East Antarctica (Fig. 1a and b). A Japanese station at Dome Fuji was built for deep ice coring. The dome summit is a wide, flat area. Based on an ERS-1 (European Remote-sensing Satellite-1) high-resolution map of Antarctica compiled by Rémy and others (1999), we estimate that the highest point on the dome plateau is 12 km west-northwest of the station; however, the elevation of the station is within 1 m of the highest point. The maximum surface slope around the station faces east-northeast. In 1996, S. Fujita and members of the Japanese Antarctic Research Expedition verified the surface slope at many sites in a 60×60 km area around Dome Fuji by ground survey. Surface ice movement rate is less than several centimeters per year at Dome Fuji (Motoyama and others, 1995). At the station, a 2503 m long ice core was drilled between 1994 and 1997 (Watanabe and others, 1999). The radar survey was carried out within 50 m of the drillhole at Dome Fuji station.

Azuma and others (1999, 2000) reported that the COF of the Dome Fuji core is a vertical single-pole pattern with cluster strength increasing with depth. However, the *c*-axis distributions do not indicate a perfect circular single maximum, but are elongated horizontally. Because of this elongation, the ice should be birefringent at radio frequencies. Azuma and others (2000) reported that the mean *c*-axis direction was always within $2 \pm 2^\circ$ from the ice-core axis, which is near vertical down to ~2000 m depth. The ice core has no geographical azimuth control, so azimuth of the elongation is not known. We tentatively assume the elongation orientation does not change dramatically with increasing depth. Later we verify this assumption by radar sounding.

Mizuho

Mizuho station is at a flank site of the Shirase Glacier drainage basin, which includes part of the inland plateau, with Dome Fuji as the highest region. The ice thickness is ~1950 m. The ice converges toward fast flow at Shirase Glacier (Fig. 1a and c). The flow vector of the ice sheet is 22.2 m a^{-1} in the direction 297° from true north (Motoyama and others, 1995). The principal strain was derived as tensile in the longitudinal direction and compression in the transverse direction (Naruse and Shimizu, 1978).

At Mizuho, a 700 m long core was drilled between 1983 and 1985 (Higashi and others, 1988). COF measurements at 12 depths showed that the *c* axes concentrated gradually on a vertical girdle with increasing depth (Narita and others, 1986; Fujita and others, 1987). The azimuth of this ice core was determined from the remnant magnetization of iron particles accidentally deposited in the drilling. By comparing the azimuth of the ice core with the azimuth of the COF cluster plane, the azimuth of the COF cluster plane was identified as perpendicular to the ice extension axis (Fujita and others, 1987).

Use of two-frequency radar measurements showed that the dominant scattering mechanism is permittivity based throughout the ice column over 300 km across the main flow of Shirase Glacier (Fujita and others, 1999, 2003; Matsuoka and others, 2003). The P_{COF} mechanism is dominant except in the top 250 m where P_D might be dominant. At depths from 250 to 750 m, the scattering is stronger when the polarization plane is along the flowline. In contrast, at depths from 900 to 1500 m, the scattering is stronger when the polarization plane is perpendicular to the flowline.

3.2. Derivation of dielectric tensor from COF data

The dielectric permittivity component of polycrystalline ice under an arbitrary external field vector can be evaluated using normalized eigenvalues of the COF (see Appendix). For the COF of the Dome Fuji ice core, Azuma and others (2000) derived the depth profile of the normalized eigenvalues. They reported that one of the principal axes of the COF was near vertical at depths shallower than 2000 m. Under the assumption that the orientation of the elongated single-pole COF did not change dramatically with increasing depth, the depth profile of the COF eigenvalues at Dome Fuji can be converted to a depth profile of the dielectric permittivity tensor. Then, for vertically propagating radio waves, we can derive the phase difference, ϕ, between waves along the two principal axes (the x wave and the y wave) as follows. Using Equation (13), the depth profile of $\left|\sqrt{\varepsilon'_x} - \sqrt{\varepsilon'_y}\right|$ is derived first from COF data (Fig. 10a). At Dome Fuji, $\left|\sqrt{\varepsilon'_x} - \sqrt{\varepsilon'_y}\right|$ is near zero at depths from the surface down to ~500 m. This is because the single-pole COF is nearly isotropic and does not show clearly elongated features. But below ~500 m, $\left|\sqrt{\varepsilon'_x} - \sqrt{\varepsilon'_y}\right|$ becomes significant and increases with increasing depth. Note that in Equation (13), $\Delta\phi_x = \Delta\phi_y$ for Dome Fuji ice because no difference in scattering

https://doi.org/10.3189/172756506781828548 Published online by Cambridge University Press

Table 3. Specifications of the VHF (very high-frequency) radar system

Carrier frequency		179 MHz	60 MHz
Transmitter	Peak power	1 kW	1 kW
	Pulse width	150 ns/350 ns/1050 ns	250 ns/1000 ns
Receiver	Sensitivity	–115 dBm*	–115 dBm
Antenna	Type	Three-element Yagi	Three-element Yagi
	Gain	8.15 dBi†	7.2 dBi
	Beam width	70° (E-plane)	60° (E-plane)
		90° (H-plane)	90° (H-plane)
Vertical resolution in ice‡		13 m/30 m/89 m	21 m/85 m
Wavelength in ice		0.94 m	2.8 m

*dBm is a unit for the power level in decibels with reference to a power of 1 mW. Receiver sensitivity assumes averaging to reduce the noise level.
†dBi is a unit for expression of antenna gain in decibels with reference to the power of an ideal isotropic antenna.
‡Vertical resolution is the wave travel distance for half the pulse width.

mechanisms has been detected between the x and y axes. Using the values of $\left|\sqrt{\varepsilon'_x} - \sqrt{\varepsilon'_y}\right|$, the total phase shift, ϕ, between x and y waves during the two-way travel is calculated at each scattering depth. The calculation has been carried out at 60 and 179 MHz. Figure 10b shows that for 179 MHz, ϕ is π, out of phase at ~1360 m depth and ϕ is 2π, at ~2150 m depth. Note that the uncertainty of $\Delta\varepsilon'$ (Equation (3)) is due to the uncertainty of these depths ~3%. Additional uncertainty arises both from the scatter of the data points in Figure 10a and from our approximation that one of the three principal axes of the COF is along the vertical. At 60 MHz, ϕ will reach π at some depth greater than 2500 m.

At Mizuho, we set the x axis to lie within the plane that contains the vertical girdle in the horizontal, y as the orthogonal horizontal direction and z as the vertical. We approximate that the vertical girdle-type COF contains the vertical. Also we assume that the vertical girdle plane does not rotate dramatically with increasing depth. For the Mizuho station ice core, Fujita and Mae (1993) calculated the depth profile of the eigenvalues. From the normalized eigenvalues of the COF, we calculate the depth profile of $\left|\sqrt{\varepsilon'_x} - \sqrt{\varepsilon'_y}\right|$ from 12 depths down to the bottom of the ice core at 700 m (Fig. 10a). The difference in the refractive index in the horizontal $\left|\sqrt{\varepsilon'_x} - \sqrt{\varepsilon'_y}\right|$ at Mizuho is much larger than at Dome Fuji (Fig. 10a). This is because the vertical girdle-type COF causes stronger birefringence. As a result, ϕ increases more rapidly at Mizuho than at Dome Fuji (Fig. 10b). At Mizuho, $\Delta\phi_x$ is not always the same as $\Delta\phi_y$. There are indications that the implied dominant scattering mechanism is P_{COF} in one orientation and C_A in another (Fujita and others, 2003). Tentatively assuming $\Delta\phi_x = \Delta\phi_y$ to avoid complexity, we derive ϕ . Later in the discussion, we check whether or not this assumption is acceptable. Figure 10b shows that at 179 MHz, ϕ is $n\pi$ at depths around 270, 420, 560 and 690 m, and possibly also at ~750 m. At 60 MHz, $\phi = \pi$ at ~560 m. Potential causes of errors are the same as for the Dome Fuji ice core.

3.3. Radar method

We use a pulse-modulated radar system to allow the effects of radar pulse length, which gives information about the vertical resolution of the signal, to be investigated. For the 179 MHz radar we used 150, 350 and 1050 ns pulses. For the 60 MHz radar we used 250 and 1000 ns. Each radar system was mounted on its own snow vehicle. The transmitting antenna T_x and the receiving antenna R_x were on opposite sides of the vehicle. The three-element Yagi antennae were either parallel to each other, i.e. co-polarization, or perpendicular, i.e. cross-polarization (Fig. 2). The specifications are given in Table 3.

For both the co-polarized and cross-polarized measurements, we measured the radar return power P_R at 16 antenna azimuths by changing the direction of the vehicle. At Dome Fuji, we rotated the antennae in steps of $\pi/8$ from 0 to 2π. At Mizuho, we rotated the antennae in steps of $\pi/16$ from 0 to π. We chose these steps ($\pi/8$ and $\pi/16$) in order to detect phenomena with a minimum periodicity of $\pi/2$. For the starting orientation, the transmitter, receiver and vehicle were oriented to true north. They were then rotated in clockwise increments. Due to the symmetry of the radio-wave propagation and scattering around the vertical, orientations from 0 to π and orientations from π to 2π were cross-checked against each other. This cross-checking was done only at Dome Fuji. The orientations were determined using a magnetic compass with errors within a few degrees for each orientation. For both co-polarized and cross-polarized measurements, antenna azimuth refers to the azimuth of the transmitting antenna.

The received power is expressed by a radar equation. A radar equation for our pulse-modulated radar system is given in section 2.4 of Matsuoka and others, (2003). Received power, P_R, decreases with increasing depth due to geometrical spreading and absorption loss of radio waves. The detection limit for the received power in the present measurements was about –115 dBm (Table 3). Also, we calibrated the system frequently and the total error in the received power is less than 1 dB, so we consider any variation in the received power that exceeds 1 dB.

The signals measured with pulse-modulated radar are often interference patterns from many scattering events within a pulse (e.g. Moore, 1988; Jacobel and Hodge, 1995). The shorter the pulse width and the fewer the scattering events in a pulse, the more clearly will signals show dominant or isolated scattering events. The vertical resolution can be defined as half the pulse width multiplied by the propagation speed of the radio wave. Echo variations at depth scales shorter than the vertical resolution are affected by many factors such as (i) exact location of the scattering objects, (ii) distance between scattering objects, (iii) type of scattering (that is, P_D, C_A or P_{COF}), (iv) orientation of the polarization plane, (v) pulse length and (vi) radar frequencies. Here we focus on the macroscopic features in radio echoes averaged over the vertical resolution.

https://doi.org/10.3189/172756506781828548 Published online by Cambridge University Press

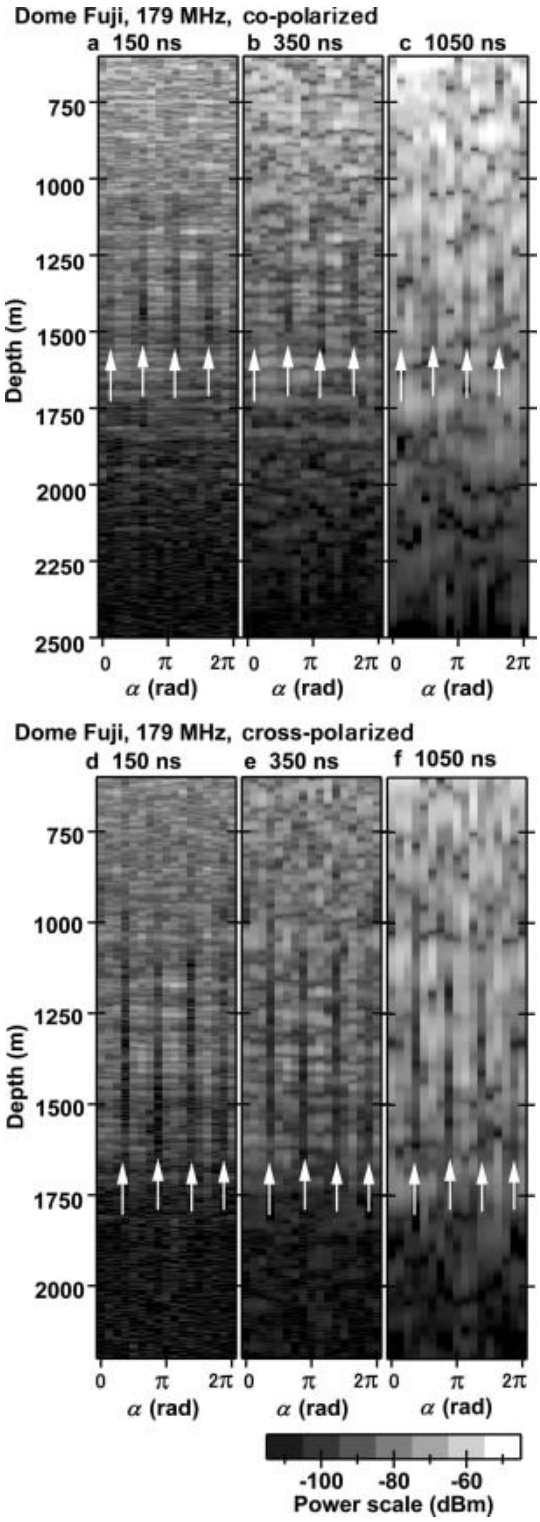

Fig. 11. Radar scattering from Dome Fuji ice obtained at 179 MHz. Antenna arrangement was co-polarization for (a–c) and cross-polarization for (d–f). Three pulse widths, 150, 350 and 1050 ns, were used for both the co-polarization and cross-polarization arrangements. The abscissa is the transmitting antenna orientation relative to true north. The ordinate is the depth of ice converted from the pulse-timing data using the propagation speed in ice. Received power, P_R (dBm), is expressed by the gray scale shown at the bottom. Strong signals are white, and weak signals are dark. Received power decreases with increasing depth due to geometrical spreading and attenuation of the radio wave. In (a–c) arrows indicate suggested co-polarization nodes with $\pi/2$ periodicity of the antenna orientation. In (d–f) the arrows mark minima with $\pi/2$ periodicity in the antenna orientation. They are suggested cross-polarization extinctions.

3.4. Results

Dome Fuji

The 179 MHz co-polarized radar data at 16 azimuths are shown in Figure 11a–c. At depths between about 1250 and 1500 m, there are distinct intensity minima as the antenna azimuth α is varied. For all pulse width data, these minima are at polarization angles $\pi/8$, $5\pi/8$, $9\pi/8$ and $13\pi/8$ (arrows in Fig. 11a–c). Thus, the signal minima occur every $\pi/2$ rad. This periodic feature is predicted to occur for birefringent ice in the model (Fig. 5a). Also, as the minima occur for all three pulse widths, it is unlikely that they are caused by accidental interference within a pulse. Although small fluctuations are probably interference effects, the average trend over depths larger than the pulse width is clear. These signal drops appear more clearly when the pulse width is shorter. In agreement with the model, the signal drops appear near depths where ϕ is expected to be π from the COF data (1360 m in Fig. 10b).

The cross-polarization measurements at 179 MHz also show periodic features. Figure 11d–f show variations of P_R with changing antenna orientations. Over a wide depth range below ~1000 m, there are extinctions of the signal at $3\pi/8$, $7\pi/8$, $11\pi/8$ and $15\pi/8$. Thus, the maxima and minima appear always at angles of $\pi/2$ where the co-polarized data have minima and maxima, respectively. These extinctions appear for all three pulse widths, as shown in Figure 11d–f. As with the co-polarization data, the extinctions appear more clearly when the pulse length is shorter.

To illustrate the variation with antenna orientation more clearly, we averaged P_R from depths of 1250–1500 m at each antenna azimuth. The data are plotted in Figure 12a and show clear periodic variations. Cross-polarized results are out of phase with the co-polarized results. We note here that measurements differing by an orientation angle $\alpha = \pi$ should have the same reflection signature (compare symmetry in Fig. 5a). The minima differ, however, by up to 8 dB between the co-polarized case and the cross-polarized case (Fig. 12a). These differences are due to small errors in antenna orientation, of up to a few degrees.

At 60 MHz, unlike the results for 179 MHz, we found little variation of P_R with changing antenna orientation for the co-polarized measurements (Fig. 13). An exception however, is the very deep ice below ~1750 m, where there are small variations of P_R with changing antenna orientation. Signal minima appear at four orientations, 0, $5\pi/8$, $8\pi/8$ and $12\pi/8$, which are always within $\pi/8$ of those in the co-polarization measurements at 179 MHz. We rejected the data for the cross-polarized measurements at 60 MHz, due to technical problems, and do not discuss them here.

Mizuho

Figure 14 shows variations of the received power with changing antenna orientations for three different experimental conditions at depths shallower than 1000 m. Figure 15 shows the data from Figure 14, averaged over four depth ranges, to depict orientations for maxima and minima at various depths. Figures 14a and 15a show the results of the co-polarization measurement at 179 MHz. A strong echo was observed when the antennae were oriented approximately along the flowline, as Fujita and others (2003) reported. Orthogonal to the flowline, the echo was weaker. We find that azimuths for the strong echo seem to rotate with depth. If we trace the orientation for the strongest

https://doi.org/10.3189/172756506781828548 Published online by Cambridge University Press

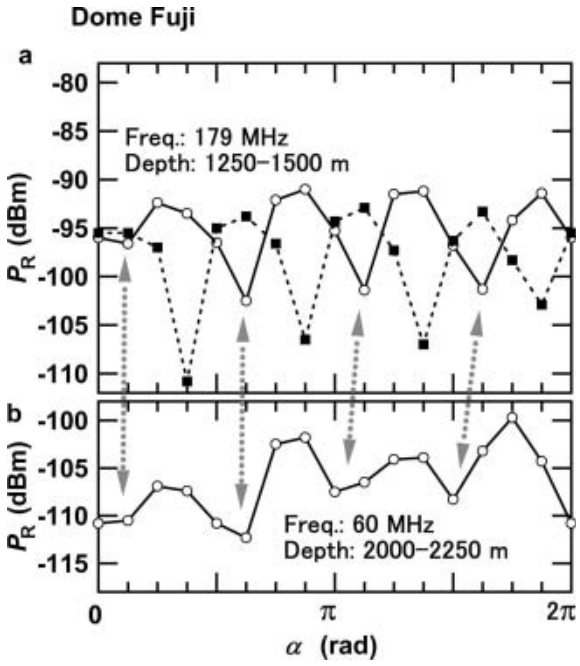

Fig. 12. Received power averaged along various antenna orientations. The solid line shows the co-polarized case and the dotted line the cross-polarized case. (a) The received power averaged over depths from 1250 to 1500 m from data collected by the 179 MHz radar with pulse width 150 ns. Both the co-polarization (Fig. 11a) and cross-polarization (Fig. 11d) results are shown. (b) The received power averaged over depths from 2000 to 2250 m collected by the 60 MHz radar with pulse width 250 ns. Only the co-polarization measurement is shown. The orientations with minima are marked by gray arrows.

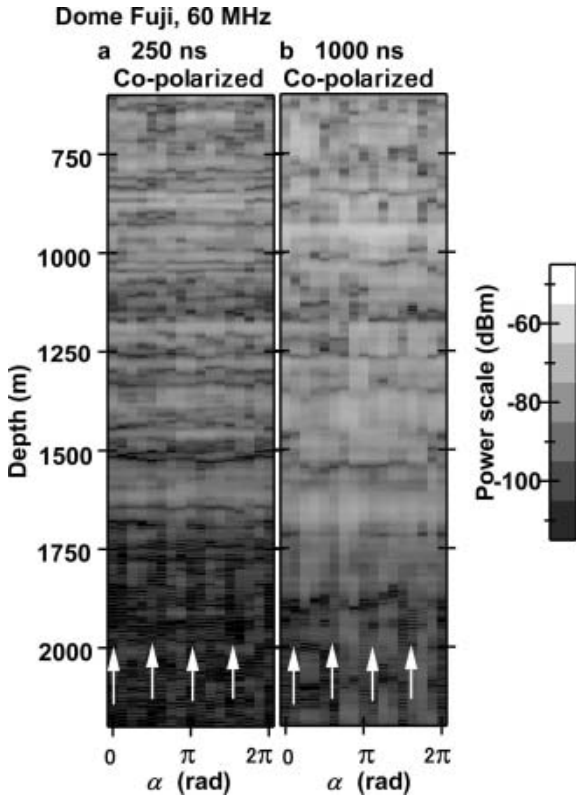

Fig. 13. Radar scattering from Dome Fuji ice obtained at 60 MHz. Antenna arrangement was co-polarization, and two pulse widths, 250 and 1000 ns, were used. The abscissa is the transmitting antenna orientation relative to true north. The ordinate is the depth of ice converted from the pulse-timing data using the propagation speed in ice. Received power, P_R (dBm), is expressed by the gray scale shown at the side. Strong signals are white, and weak signals are dark. Received power decreases with increasing depth due to geometrical spreading and attenuation of the radio wave. Arrows mark apparent signal minima with $\pi/2$ periodicity of antenna orientation. These appear clearly when the data are averaged, shown in Figure 12b.

signals (dotted line in Figs 14a and 15a), the range of the variation is about $\pi/4$.

Figures 14b and 15b show the results of the cross-polarization measurement at 179 MHz. Over a wide depth range, there are signal minima at two orientations as shown by the dotted lines. The maxima between the minima are of different magnitudes. As with the co-polarization data, the cross-polarization data form meandering curves that approximately follow the flowline and the orthogonal orientations. In addition, the variation of the orientations with depth is similar to the co-polarization case in Figures 14a and 15a. Black arrows in Figures 14 and 15 are the co-polarization node and suggested ridge, respectively. They are discussed below.

In the co-polarized measurements at 60 MHz, strong echoes occur at two orientations, the flowline and the orthogonal orientation shown as dotted lines along the approximate maxima in Figures 14c and 15c. The curves in the 60 MHz data appear straighter than those for 179 MHz. We also see clear high-resolution minima and maxima, just 10–30 m wide, for 60 MHz, 250 ns in Figure 14c. Because these features are much finer than those the model simulated as nodes, we believe they come solely from fluctuation of the internal reflections with depth.

3.5. Discussion and interpretation

Features indicating birefringence at Dome Fuji

At Dome Fuji the observed features indicate birefringence in the ice sheet. For example, for the 179 MHz co-polarization measurement, the signal minima appear when ϕ is expected to be an odd multiple of π (at 1360 m in Fig. 10b). This signal drop is the co-polarization node predicted by our model analysis (Fig. 5; Table 2). Another example is from the 179 MHz cross-polarization measurement. The signal extinction over a wide depth range with periodicity $\pi/2$ is typical for a pure birefringent medium and/or anisotropy at the scattering boundaries, again predicted by the model. They appear when the cross-polarized antennae are oriented along the principal axes of birefringence or the scattering anisotropy and are cross-polarization extinctions (Table 2). According to the model, a single cross-polarization measurement is not sufficient for distinguishing between the cross-polarization extinction caused by birefringence and that caused by anisotropic scattering. However, in the present case, we have already observed the co-polarization node, although not of equal minimum magnitude. This means that the cross-polarization extinction is caused by birefringence. Further features that indicate birefringence are the nodes that were observed in the 60 MHz co-polarization measurement. According to Figure 10b, ϕ reaches close to π at ~2500 m depth. We propose that the minima in the 60 MHz co-polarization measurements are a shallow tail of the co-polarization node centered at ~2500 m depth.

https://doi.org/10.3189/172756506781828548 Published online by Cambridge University Press

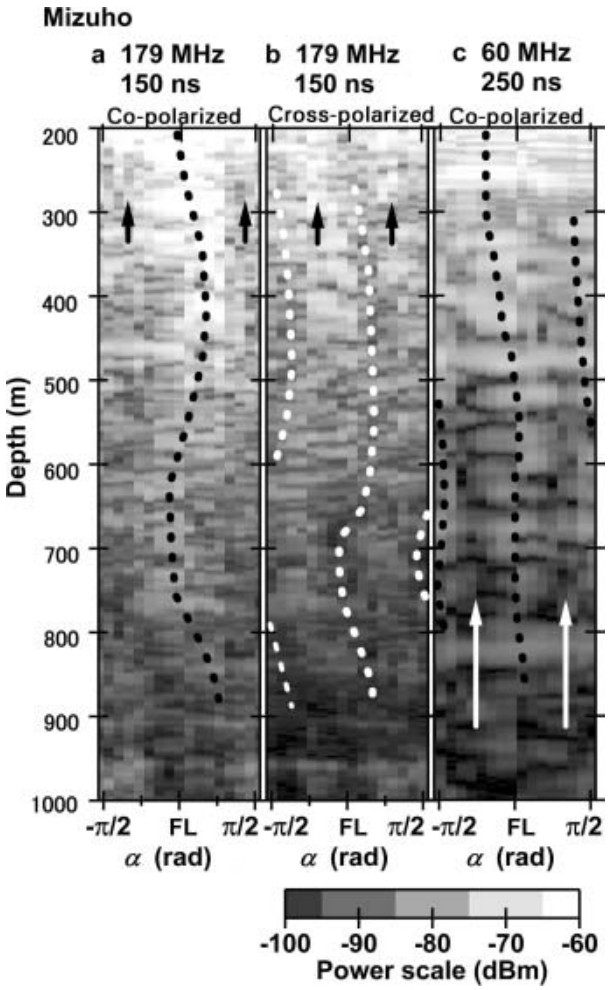

Fig. 14. Radar scattering from the ice sheet at Mizuho station. Panels are adapted from figures 6, 8 and 9 of Fujita and others (2003). The abscissa is the transmitting antenna orientation relative to the flowline (FL). Unlike Figures 11 and 13, here the abscissa spans only π. The flowline is from 117° to 279° from true north. The ordinate is the depth of ice converted from the pulse-timing data. Received power, P_R (dBm), is expressed by the gray scale shown at the bottom. Frequency, pulse width and antenna configuration are shown for each panel. The dotted lines in (a–c) were drawn by hand and are discussed in the text. Arrows in (a) and (b) are the suggested co-polarization node and the suggested ridge at 270 m, respectively. Arrows in (c) are the suggested orientation of the co-polarization node.

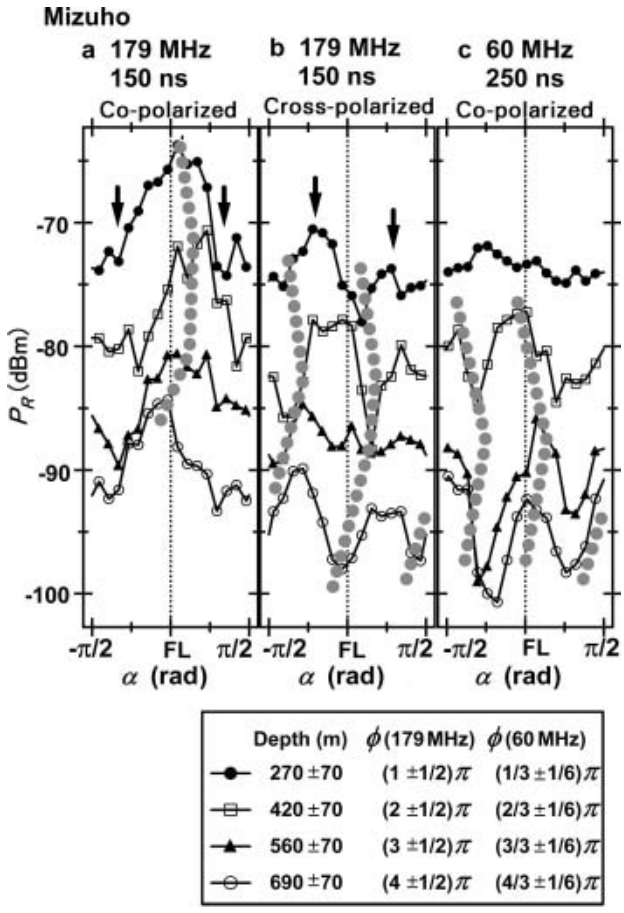

Fig. 15. Maxima and minima at various depths at Mizuho station. The curves are based on data from Figure 14 with the specifications shown in the legend. The abscissa span is again only π. The received power, P_R, is averaged over four depth ranges where ϕ is expected to be an integer multiple of π at 179 MHz (Fig. 10). The averaging distance is 140 m for each curve. Because this averaging distance is much larger than a pulse width in ice (Table 3), the averaged values show a mean tendency of signal variation of P_R. The dotted gray lines in (a–c) were marked by hand. The dotted gray lines in (b) are the suggested points of cross-polarization extinction. Arrows in (a) and (b) are the suggested co-polarization nodes and ridges, respectively, at 270 m.

We observed both the co-polarization nodes and the cross-polarization extinction. A further typical feature for the birefringence is the cross-polarization node, which can appear in the cross-polarization measurement. The cross-polarization node, from the model, is a signal minimum at every 2π of ϕ at the antenna rotation angle $\pi/4$ away from the principal axes. We demonstrate below that the third feature, a cross-polarization node, is also present in the data.

Orientation of elongated COF

From the variation of the signals, we can determine the orientations for the principal axes of COF at Dome Fuji. They are along the cross-polarization extinction ($\theta = 0$, $\pi/2$, π, ...) and $\pi/4$ rad away from the co-polarization nodes. Based on data from Figures 11–13, the principal axes are along the $3\pi/8$ to $11\pi/8$ axis and the $7\pi/8$ to $15\pi/8$ axis. At depths below ~1750 m, the principal axes are slightly deviated anticlockwise by up to $\pi/8$. This is an indication that the geographical orientation of the principal axes is not exactly constant with depth. The direction of the maximum surface slope around the station is east-northeast ($3\pi/8$ to $11\pi/8$ axis), coincident with one of the principal axes. Considering the relations between ice flow and COF formation, we can interpret the orientations for the long axis and short axis of the elongated single pole. The major strain component in an ice-divide area like Dome Fuji is longitudinal extension in the flow direction. Since the ice-crystal glide plane is perpendicular to the *c* axis, we can expect the *c* axes to cluster more along the transverse orientation than along the longitudinal orientation. Another possibility is simple shear strain in the flow direction. Either of these or a superposition of them suggests that the long axis of the single pole will be perpendicular to the flow direction.

Anisotropy in COF

To further extract features of birefringence from the 179 MHz co-polarization data, we average the radar profiles over 4 of

https://doi.org/10.3189/172756506781828548 Published online by Cambridge University Press

the 16 orientations that have co-polarization nodes. These orientations are $\pi/8$, $5\pi/8$, $9\pi/8$ and $13\pi/8$. Then we compare the result with the average of the radar profiles over four orientations that have the strongest signals, i.e. along the principal axes. These orientations include $3\pi/8$, $7\pi/8$, $11\pi/8$ and $15\pi/8$. On the decibel scale, this is

$$\delta P_{\mathrm{R}} = \frac{1}{4}\sum_{i=1}^{4}\left\{P_{\mathrm{R}}\left[\frac{\pi(4i-3)}{8}\right]\right\} - \frac{1}{4}\sum_{i=1}^{4}\left\{P_{\mathrm{R}}\left[\frac{\pi(4i-1)}{8}\right]\right\}. \quad (14)$$

Figure 16a shows the result. The curve shows a minimum at a depth where ϕ reached π as a co-polarization node (Fig. 16a). This depth of the signal drop agrees well with depth calculated from the COF (Fig. 10). In addition, at a depth where $\phi = 2\pi$, as calculated from the COF, the value of δP_{R} is near zero. These features are in good agreement with the model (see Fig. 7).

We did a similar analysis on the 179 MHz cross-polarized data. We calculated an average of the radar profiles over 4 of the 16 orientations that have the strongest signals ($\pi/8$, $5\pi/8$, $9\pi/8$ and $13\pi/8$). This average was compared with an average over four orientations that gave cross-polarization extinction ($3\pi/8$, $7\pi/8$, $11\pi/8$ and $15\pi/8$) along the principal axes. Figure 16b shows the resulting δP_{R}. The phase of signal increase and drop is opposite to the co-polarization case. When $\phi = \pi$ and $\phi = 2\pi$, the difference shows maxima and minima, respectively. This minimum is verification for the third piece of evidence for birefringence, the cross-polarization node suggested above.

Similar analysis was carried out for the 60 MHz co-polarization data. The method was the same as for the 179 MHz co-polarization data. The result, in Figure 16c, suggests that the deepest depth (2300 m) was not sufficient for ϕ to reach π. This is consistent with the shallow tail of the co-polarization nodes that was discussed above.

Because of the good agreement between theory and the radar data analyses, including our assumption of a depth-independent direction of the elongated COF, we conclude that our tentative assumption was basically correct. That is, the orientation for the elongation of the single-pole COF pattern did not vary with depth. However, at depths below ~1750 m, the principal axes can be slightly deviated anticlockwise by up to $\pi/8$. This is a fact that we need to consider when interpreting dynamical conditions at the Dome Fuji ice-coring site.

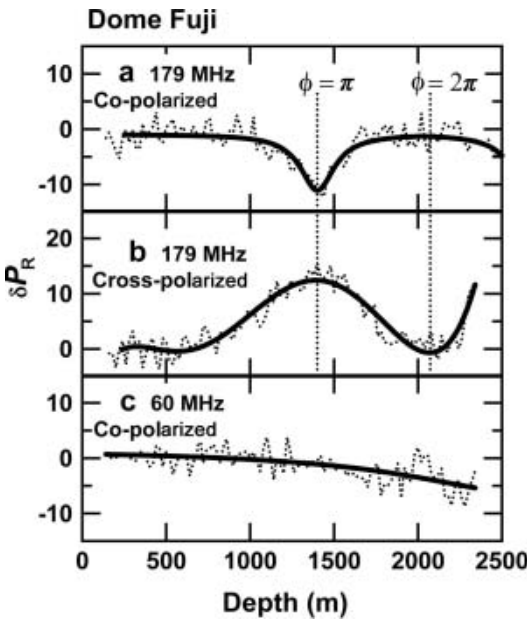

Fig. 16. Variations of δP_{R} defined by Equation (14) calculated for radar data at Dome Fuji. (a) Radar frequency 179 MHz, pulse width 150 ns and co-polarization configuration. The dotted line shows data averaged over each 20 m depth range, which is slightly longer than the 13 m long pulse width (Table 3). The thick line is a fitted line. For data at depths below 2000 m, radar data with a pulse width of 1 μs are shown to complement the depth range that cannot be detected with the 150 ns pulse width. (b) Analysis of cross-polarized data from Figure 11d–f. Frequency 179 MHz and pulse width 150 ns. (c) Frequency 60 MHz, pulse width 250 ns and co-polarization configuration.

Potential of the radar method to infer ice dynamics near a dome summit

Ritz and others (2001) studied the time evolution of the Antarctic ice sheet over long time periods using a thermomechanical three-dimensional (3-D) ice-sheet model. They estimated that the altitude of the ice-sheet surface at inland sites located on the Antarctic plateau changed commonly by ~150 m in the glacial–interglacial periods. For ice-core studies like the Dome Fuji ice core, it is important that ice-coring sites are located near the summit. To better interpret ice-core age at each depth, we are interested in how the highest position of Dome Fuji migrated historically in glacial–interglacial periods. The long-term change of the Antarctic ice sheet may have changed not only the elevation but also the summit position.

Our observations suggest that the geographical orientations of the principal axes for COF are constant to depths down to ~2200 m, with possible deviation of up to $\pi/8$ below ~1750 m. Such information is currently unavailable from ice-core studies; it is information only radar sounding can find. The next important problem concerns interpretation of the radar sounding for COF. To infer strain history of ice from COF, we need to understand the relation between ice flow and COF over very long timescales. This topic requires extensive discussion and is beyond the scope of this paper. Nevertheless, a tempting potential of the radar method is to infer the ice dynamics over wide areas near dome summits.

Birefringence and scattering at Mizuho

A clear feature of the 179 MHz co-polarization data from Mizuho is that a strong echo is oriented nearly along the flowline but rotated by up to $\pi/4$ from one depth to another (Fig. 14a). This means that the anisotropic scattering boundaries have principal axes that rotate back and forth with increasing depth. This seems an important example of rotation of principal axes of COF due to different strain history from one depth to another. The cross-polarization extinction, observed over a wide depth range with periodicity $\pi/2$, is consistent with a return signal that is dominated by anisotropic scattering. Moreover, the cross-polarization extinction, also from 179 MHz, supports the argument that the axes of the anisotropic scattering boundaries rotate by up to $\pi/4$ from one depth to another. However, the signal variation with periodicity, $\pi/2$ in the 60 MHz co-polarization data, is typical for a birefringent medium. Fujita and others (2003) proposed the following interpretation of this finding.

https://doi.org/10.3189/172756506781828548 Published online by Cambridge University Press

At 179 MHz, radar signals are strongly controlled by anisotropic scattering boundaries with anisotropy as large as 10 dB (e.g. Fig. 14a). At 179 MHz, the major cause of the radio scattering showing strong anisotropy is P_{COF}. At 60 MHz, the major causes of the radio-wave scattering at Mizuho are both P_{COF} and C_A, because C_A-based scattering is stronger at lower frequencies. The findings here support this argument.

Although the COF in Figure 10 suggests there is a strong birefringence effect at Mizuho, we did not find any clear co-polarization or cross-polarization node in the radar data, unlike the situation at Dome Fuji. In line with our theoretical analyses of radar echo from anisotropic scattering with birefringence, we sought features in the radar data in Figures 14 and 15 in several ways, but did not find convincing features of birefringence in the data.

According to the theory, when birefringence and anisotropic scattering are combined the co-polarization and cross-polarization nodes become unclear. The theory can explain the observational fact. But another reason why features in the data can become obscured is the existence of an orientation-dependent scattering mechanism. If the anisotropic scattering mechanism P_{COF} and isotropic mechanism C_A are distributed and mixed in ice sheets with comparable magnitudes, both phase and amplitude of the scattered radio wave may become difficult to interpret. In Equation (13) the term $(\Delta\phi_x - \Delta\phi_y)$ is not only non-zero but also fluctuates. It is plausible, then, that small-scale features like the co-polarization and the cross-polarization nodes might disappear due to fluctuations in both amplitude and phase. In such a case, to evaluate effects from the P_{COF} mechanism and the C_A mechanism, an effective experimental method is to use radio frequencies lower than 60 MHz and higher than 179 MHz. Then we can further analyze the relative contribution of these scattering mechanisms.

4. SUMMARY

To better understand polarimetric multi-frequency radar data, we developed a matrix model of radio-wave propagation within birefringent ice including anisotropic scattering surfaces. The model can accommodate many of the presently known properties of polar ice sheets. These properties include birefringence caused by COF, isotropic scattering caused by the P_D and C_A mechanisms, and anisotropic scattering caused by the P_{COF} mechanism. In addition, our matrix-based model is easily expandable using ice-core-based permittivity and conductivity data. Thus the model is a practical tool to link radar and ice-core research. We simulated the effect of birefringence, anisotropic scattering and combined effects from these two. We also described the detection of major features caused by interference between waves along two principal axes at the receiving antenna. The most distinct features are the co-polarization node, the cross-polarization node and the cross-polarization extinction (Fig. 5).

Using this model, we suggested how common birefringence effects may appear in VHF (very high-frequency) radar sounding of polar ice sheets. When the radar frequency is higher or when the COF anisotropy is stronger in the horizontal plane, the birefringent effects appear at shallower depths. In addition, we assessed how the multi-frequency method can be used to distinguish permittivity-based reflections from conductivity-based reflections within the birefringent ice. The calculations suggest that the birefringence gives an identifiable effect, and hence polarimetric radar sounding can be used to distinguish between the birefringence and frequency-dependent scattering.

When birefringence is dominant, the polarimetric radar method can determine the strength of the birefringence and the direction of the principal axes. When anisotropic scattering is dominant, the polarimetric radar method can indicate how the strength and orientation of the COF change with depth. In addition, if two or more frequencies are used for a radar survey, one can get further insights into the depth profile of birefringence and the scattering mechanisms.

We verified that many of the model-simulated features are found in the real radar data. We examined radio-wave depolarization and scattering at two contrasting inland sites on the Antarctic ice sheet. The radar data were supplemented with COF data that had previously been obtained from deep ice cores. We summarize the major results from the experiments as follows.

Dome Fuji was shown to be an example of a birefringent ice sheet. The data demonstrated three major features of a birefringent medium: co-polarization node, cross-polarization extinction and cross-polarization node. The depths of these features were consistent with the COF of the ice core.

We determined the principal axes of the COF at Dome Fuji station, and found them to be along the orientation of the maximum surface slope and the orthogonal orientation. The principal axes of the COF at Dome Fuji were similar throughout the depth range of ~500 to 2200 m, the latter being the greatest depth studied. At depths below ~1750 m, the principal axes can be slightly deviated anticlockwise by up to $\pi/8$.

Ice in a convergent and faster-flowing condition was examined at Mizuho. The radar data at Mizuho appeared to exhibit the combined effects of birefringence and anisotropic scattering. In response to antenna azimuth, we found there were periodic changes over π and $\pi/2$, regardless of depth. We also observed a cross-polarization extinction. However, the depth-dependent minor features like the co-polarization and cross-polarization nodes were not clearly found in the radar data. The theory showed that the co-polarization and cross-polarization nodes become unclear when birefringence and anisotropic scattering are combined. In addition, the observations at Mizuho suggested that amplitude and phase can fluctuate due to orientation-dependent scattering mechanisms. Such conditions obscure the small-scale features like the co-polarization and the cross-polarization nodes. In this way, the data still suggest information about conditions within the ice sheet.

Importantly, the verification of the theoretical analyses by comparison with experiments strongly supports the polarimetric radar method as a powerful tool to explore COF within ice. Our method should apply to a wide range of ice sheets. Indeed, a ground-based radar survey by Matsuoka and others (2003) found that birefringent features appear strongly at many inland sites, not only near domes or ridges but also in areas far from either. Matsuoka and others (2003) also found that the anisotropic scattering features appear strongly at many sites in convergent flow conditions. In this way, ice-sounding radar can detect stress–strain configuration over a wide area and over a range of depths. At sites like Mizuho, we detect periodic co-polarization changes of radar signal over π and $\pi/2$ and clear cross-polarization extinction, which reveals stress–strain configuration. Polarimetric radar

https://doi.org/10.3189/172756506781828548 Published online by Cambridge University Press

sounding over a wide area should allow reconstruction of 3-D information on the ice-sheet dynamics. In addition, if a dome summit or ridge migrated during glacial–interglacial cycles and if strain history memory in COF is not erased, one should be able to detect the migration through analysis of the COF in ice. A further step in the present work is to apply this radar method to a number of sites over dome summit plateaus and sites along traverses. Also, the strengths and limitations of COF as a memory of strain history need extensive study.

Finally, we suggest some recommendations for future measurements in polarimetric multi-frequency radar surveys. Minimum periodicity of the birefringent phenomena is $\pi/2$. Considering that at least four data points are necessary to detect this cycle, the recommended sampling step for antennae orientation is $\pi/8$ or less. We demonstrated that a shorter pulse gave a clearer result. But a shorter pulse in pulse-modulated radar implies the detection limit depth is smaller. We therefore need to compromise between clarity and detection depth depending on the depth range under investigation. We recommend that two or more pulse widths be used for a single site. Because frequency affects both dominant scattering mechanisms (e.g. Fujita and Mae, 1994; Fujita and others 2000; Matsuoka and others, 2003) and depth of co-polarization nodes and cross-polarization nodes as in Figure 6, we cannot make general recommendations. We used 60 and 179 MHz, but many other frequencies, in particular lower and higher frequencies, need to be explored.

ACKNOWLEDGEMENTS

This paper is a contribution to the Dome Fuji Project, a program conducted by the Japanese Antarctic Research Expedition. We are grateful to T. Kozu and T. Furukawa for contributions to the theory and radar measurements, respectively. This paper was first submitted to *Annals of Glaciology* in 2003. We thank all the editors and reviewers who have contributed to improvements in this paper: V. Lytle as a scientific editor of *Annals of Glaciology*, T.H. Jacka as chief and scientific editor of *Journal of Glaciology*, O. Eisen, P. Gogineni and four anonymous reviewers. Their critical reviews have improved this paper greatly. We thank N. Azuma for providing us with the COF dataset from the Dome Fuji station ice core. Participation of K.M. was supported by US National Science Foundation grant OPP-0338151.

REFERENCES

Ackley, S.F. and T.E. Keliher. 1979. Ice sheet internal radio-echo reflections and associated physical property changes with depth. *J. Geophys. Res.,* **84**(B10), 5675–5680.

Arcone, S.A., V.B. Spikes and G.S. Hamilton. 2005. Phase structure of radar stratigraphic horizons within Antarctic firn. *Ann. Glaciol.,* **41**, 10–16.

Azuma, N. 1994. A flow law for anisotropic ice and its application to ice sheets. *Earth Planet. Sci. Lett.,* **128**(3–4), 601–614.

Azuma, N. *and 6 others*. 1999. Textures and fabrics in the Dome F (Antarctica) ice core. *Ann. Glaciol.,* **29**, 163–168.

Azuma, N. *and 6 others*. 2000. Crystallographic analysis of the Dome Fuji ice core. *In* Hondoh, T., *ed. Physics of ice core records*. Sapporo, Hokkaido University Press, 45–61.

Bogorodsky, V.V., C.R. Bentley and P.E. Gudmandsen. 1985. *Radioglaciology*. Dordrecht, etc., D. Reidel Publishing Co.

Budd, W.F. and T.H. Jacka. 1989. A review of ice rheology for ice sheet modelling. *Cold Reg. Sci. Technol.,* **16**(2), 107–144.

Doake, C.S.M. 1981. Polarization of radio waves in ice sheets. *Geophys. J. R. Astron. Soc.,* **64**(2), 539–558.

Doake, C.S.M., H.F.J. Corr and A. Jenkins. 2002. Polarization of radio waves transmitted through Antarctic ice shelves. *Ann. Glaciol.,* **34**, 165–170.

Eisen, O., F. Wilhelms, U. Nixdorf and H. Miller. 2003. Identifying isochrones in GPR profiles from DEP-based forward modeling. *Ann. Glaciol.,* **37**, 344–350.

Fujita, S. and S. Mae. 1993. Relation between ice sheet internal radio-echo reflections and ice fabric at Mizuho Station, Antarctica. *Ann. Glaciol.,* **17**, 269–275.

Fujita, S. and S. Mae. 1994. Causes and nature of ice-sheet radio-echo internal reflections estimated from the dielectric properties of ice. *Ann. Glaciol.,* **20**, 80–86.

Fujita, S., M. Nakawo and S. Mae. 1987. Orientation of the 700-m Mizuho core and its strain history. *Proceedings of the NIPR Symposium on Polar Meteorology and Glaciology*, 1, 122–131.

Fujita, S. *and 6 others*. 1999. Nature of radio-echo layering in the Antarctic ice sheet detected by a two-frequency experiment. *J. Geophys. Res.,* **104**(B6), 13,013–13,024.

Fujita, S., T. Matsuoka, T. Ishida, K. Matsuoka and S. Mae. 2000. A summary of the complex dielectric permittivity of ice in the megahertz range and its applications for radar sounding of polar ice sheets. *In* Hondoh, T., *ed. Physics of ice core records*. Sapporo, Hokkaido University Press, 185–212.

Fujita, S., H. Maeno, T. Furukawa and K. Matsuoka. 2002. Scattering of VHF radio waves from within the top 700 m of the Antarctic ice sheet and its relation to the depositional environment: a case-study along the Syowa–Mizuho–Dome Fuji traverse. *Ann. Glaciol.,* **34**, 157–164.

Fujita, S., K. Matsuoka, H. Maeno and T. Furukawa. 2003. Scattering of VHF radio waves from within a an ice sheet containing the vertical-girdle-type ice fabric and anisotropic reflection boundaries. *Ann. Glaciol.,* **37**, 305–316.

Gogineni, S., T. Chuah, C. Allen, K. Jezek and R.K. Moore. 1998. An improved coherent radar depth sounder. *J. Glaciol.,* **44**(148), 659–669.

Hargreaves, N.D. 1977. The polarization of radio signals in the radio echo sounding of ice sheets. *J. Phys. D,* **10**(9), 1285–1304.

Hargreaves, N.D. 1978. The radio-frequency birefringence of polar ice. *J. Glaciol.,* **21**(85), 301–313.

Higashi, A., M. Nakawo, H. Narita, Y. Fujii, F. Nishio and O. Watanabe. 1988. Preliminary results of analyses of 700 m ice cores retrieved at Mizuho Station, Antarctica. *Ann. Glaciol.,* **10**, 52–56.

Jacobel, R.W. and S.M. Hodge. 1995. Radar internal layers from the Greenland summit. *Geophys. Res. Lett.,* **22**(5), 587–590.

Kanagaratnam, P., S.P. Gogineni, N. Gundestrup and L. Larsen. 2001. High-resolution radar mapping of internal layers at the North Greenland Ice Core Project. *J. Geophys. Res.,* **106**(D24), 33,799–33,811.

Kohler, J., J.C. Moore and E. Isaksson. 2003. Comparison of modelled and observed responses of a glacier snowpack to ground-penetrating radar. *Ann. Glaciol.,* **37**, 293–297.

Lipenkov, V.Y. and N.I. Barkov. 1998. Internal structure of the Antarctic ice sheet as revealed by deep core drilling at Vostok station. *In Lake Vostok study: scientific objectives and technological requirements. International workshop. Abstracts*. St Petersburg, Arctic and Antarctic Research Institute, 31–35.

Lipenkov, V.Y., N.I. Barkov, P. Duval and P. Pimienta. 1989. Crystalline texture of the 2083 m ice core at Vostok Station, Antarctica. *J. Glaciol.,* **35**(121), 392–398.

Matsuoka, T., S. Fujita, S. Morishima and S. Mae. 1997. Precise measurement of dielectric anisotropy in ice Ih at 39 GHz. *J. Appl. Phys,* **81**(5), 2344–2348.

Matsuoka, T., S. Mae, H.Y. Fukazawa, S. Fujita and O. Watanabe. 1998. Microwave dielectric properties of the ice core from Dome Fuji, Antarctica. *Geophys. Res. Lett.,* **25**(10), 1573–1576.

https://doi.org/10.3189/172756506781828548 Published online by Cambridge University Press

Matsuoka, K. *and 6 others*. 2003. Crystal-orientation fabrics within the Antarctic ice sheet revealed by a multi-polarization-plane and dual frequency radar survey. *J. Geophys. Res.,* **108**(B10), 2499. (10.1029/2002JB002425.)
Matsuoka, K., S. Uratsuka, S. Fujita and F. Nishio. 2004. Ice-flow induced scattering zone within the Antarctic ice sheet revealed by high-frequency airborne radar. *J. Glaciol.,* **50**(170), 382–388.
Miners, W.D., A. Hildebrand, S. Gerland, N. Blindow, D. Steinhage and E.W. Wolff. 1997. Forward modeling of the internal layers in radio echo sounding using electrical and density measurements from ice cores. *J. Phys. Chem. B.* **101**(32), 6201–6204.
Miners, W.D., E.W. Wolff, J.C. Moore, R. Jacobel and L. Hempel. 2002. Modeling the radio echo reflections inside the ice sheet at Summit, Greenland. *J. Geophys. Res.,* **107**(B8, 2172). (10.1019/2001JB000535.)
Moore, J.C. 1988. Dielectric variability of a 130 m Antarctic ice core: implications for radar sounding. *Ann. Glaciol.,* **11**, 95–99.
Moore, J.C. and S. Fujita. 1993. Dielectric properties of ice containing acid and salt impurity at microwave and low frequencies. *J. Geophys. Res.,* **98**(B6), 9769–9780.
Motoyama, H. *and 8 others*. 1995. Preliminary study of ice flow observations along traverse routes from coast to Dome Fuji, East Antarctica by differential GPS method. *Antarct. Rec.,* **39**, 94–98.
Narita, H., M. Nakawo and Y. Fujii. 1986. Textures and fabrics of 700-m deep ice core obtained at Mizuho Station, East Antarctica. *Nat. Inst. Polar Res. Mem.,* 45 Special Issue, 74–77.
Naruse, R. and H. Shimizu. 1978. Flow line of the ice sheet over Mizuho Plateau. *Nat. Inst. Polar Res. Mem.* 7, Special issue, 227–234.
Nixdorf, U. *and 6 others*. 1999. The newly developed airborne radio-echo sounding system of the AWI as a glaciological tool. *Ann. Glaciol.,* **29**, 231–238.
Rémy, F., P. Shaeffer and B. Legrésy. 1999. Ice flow physical processes derived from ERS-1 high-resolution map of Antarctica and Greenland ice sheet. *Geophys. J. Int.,* **139**(3), 645–656.
Ritz, C., V. Rommelaere and C. Dumas. 2001. Modeling the evolution of Antarctic ice sheet over the last 420,000 years: implications for the altitude changes in the Vostok region. *J. Geophys. Res.,* **106**(D23), 31,943–31,964.
Robin, G.deQ., S. Evans and J.T. Bailey. 1969. Interpretation of radio echo sounding in polar ice sheets. *Philos. Trans. R. Soc. London, Ser., A.* **265**(1166), 437–505.
Stutzman, W.L. 1992. *Polarization in electromagnetic systems.* Norwood, MA, Artech House.
Ulaby, F.T. and C. Elachi. 1990. *Radar polarimetry for geoscience applications.* Norwood, MA, Artech House.
Ulaby, F.T., R.K. Moore and A.K. Fung. 1981. *Microwave remote sensing, active and passive. Vol. 1. Fundamentals and radiometry.* Reading, MA, Addison-Wesley Publishing Co.
Watanabe, O., K. Kamiyama, H. Motoyama, Y. Fujii, H. Shoji and K. Satow. 1999. The palaeoclimate record in the ice core from Dome Fuji station, Antarctica. *Ann. Glaciol.,* **29**, 176–178.

APPENDIX

DERIVATION OF DIELECTRIC TENSOR FROM COF DATA

The *c* axes of ice-sheet ice have various orientations in space. When the angle between the external electrical field and the *c* axis is φ, the component of dielectric permittivity projected along the electrical field is

$$\varepsilon'(\varphi) = \left(\varepsilon'_{\perp}{}^{2}\sin^2\varphi + \varepsilon'^{2}_{\parallel}\cos^2\varphi\right)^{1/2}. \quad \text{(A1)}$$

The dielectric permittivity component of polycrystalline ice under an arbitrary external field vector can be evaluated as a mixture of different dielectrics, these being the individual crystals, each having a different dielectric permittivity tensor due to their differing orientations. Hargreaves (1978) derived the macroscopic dielectric tensor $\boldsymbol{\varepsilon}'$ as

$$\boldsymbol{\varepsilon}' = \sum_{j=1} f_j \varepsilon^{(j)}, \quad \text{(A2)}$$

where $\varepsilon^{(j)}$ and f_j are the dielectric permittivity tensor and volume fraction of each (jth) crystal in a total volume. To calculate the depth profile of $\boldsymbol{\varepsilon}'$ from ice-core data, the volume should be a piece of polycrystalline ice. Both $\varepsilon^{(j)}$ and f_j should be determined for each crystal.

In a birefringent medium, we are interested in the phase difference between two wave components each along two principal axes in the horizontal plane. Hereafter, we call these two components *x* wave and *y* wave. Ice sheets are biaxial, not uniaxial, so that both the *x*- and *y*-wave components are extraordinary waves. For radar sounding of ice sheets, we discuss only radio waves propagating vertically. Thus, we do not consider the electrical field along *z*. We consider the electrical field along *x* and *y* only.

To express COF using a macroscopic tensor, some recent COF studies introduced normalized eigenvalues (e.g. Azuma and others, 2000). Normalized eigenvalues range from 0 to 1. Each tensor component is a component of the *c* axis projected along each of the three principal axes. The normalized eigenvalues are E_1, E_2 and E_3. The principal axes of a COF are, in principle, independent of the orthogonal coordinates *x*, *y* and *z* of the ice sheet. However, when E_3 is very close to *z*, as in polar ice sheets, we can estimate that E_3 is along the vertical and the two other axes, E_1 and E_2, are on the horizontal. If both E_1 and E_2 are on the horizontal, then the depth profile of the dielectric permittivity tensor along the three principal axes is expressed using the normalized eigenvalues as:

$$\boldsymbol{\varepsilon}'(z) = \begin{pmatrix} \varepsilon'_x & 0 & 0 \\ 0 & \varepsilon'_y & 0 \\ 0 & 0 & \varepsilon'_z \end{pmatrix}$$

$$= \begin{pmatrix} \varepsilon'_{\perp} + \Delta\varepsilon' E_1 & 0 & 0 \\ 0 & \varepsilon'_{\perp} + \Delta\varepsilon' E_2 & 0 \\ 0 & 0 & \varepsilon'_{\perp} + \Delta\varepsilon' E_3 \end{pmatrix}. \quad \text{(A3)}$$

MS received 28 October 2005 and accepted in revised form 31 July 2006